# *A nanobody-based approach to capture and visualize interactions of binary protein complexes in living cells*

Nawal HAJJ SLEIMAN[1], Julie CARNESECCHI[1,2], Yunlong JIA[3], Fréderic DELOLME[4], Laurent GILQUIN[1], Patrice Gouet[4] and Samir MERABET[1,#]

[1]*Institut de Génomique Fonctionnelle de Lyon, Centre National de Recherche Scientifique, Ecole Normale Supérieure de Lyon, Lyon, France.*

[2]*Institut de Génétique Moléculaire de Montpellier, Centre National de Recherche Scientifique, University of Montpellier, Montpellier, France.*

[3]*Department of Developmental and Cellular Biology, University of California Irvine, Irvine, CA 92697, USA.*

[4]*Protein Science Facility, SFR BioSciences, CNRS, UMS3444, Lyon, France.*

*#corresponding author: samir.merabet@ens-lyon.fr*

**Abstract**

Protein function depends on interactions with other protein partners, ultimately leading to the formation of intricate protein-protein interaction (PPI) networks. These molecular networks (or interactomes) are formed progressively, each interaction influencing the next one. Accordingly, a same protein can lead to the formation of different interactomes depending on its first associated cofactor. Therefore, capturing PPIs of specific dimeric protein complexes is key for understanding the molecular rules underlying the diverse cell- and/or subcellular-functions of a bait protein of interest. Here, we introduce an innovative method called Bi-nano-ID that is based on bicolor bimolecular fluorescence complementation and the specific binding of a nanobody fused to a proximity-dependent biotinylating enzyme to tackle this issue. Bi-nano-ID was used to capture endogenous interactomes of the cytoplasmic TAZ/14-3-3e and nuclear TAZ/TEAD2 complexes, which are major downstream effectors of the Hippo signaling pathway. Among the different specific interactions, we revealed the role of a particular family of protease inhibitors for stabilizing and promoting the proliferative activity of TAZ/14-3-3e complexes in mesenchymal stem cells. Overall, our work establishes a novel sensitive method for capturing and visualizing specific interactions of binary bait protein complexes in human living cells.

**Key words:** Bi-nano-ID, BiFC, GFP-nanobody, TurboID, TAZ, Hippo

## Introduction

Proteins are not working individually within the cell environment, but by forming connected networks, or interactomes, with other protein-binding partners. These molecular networks are established by successive protein-protein interactions (PPIs) and can vary depending on the cell type and/or cell compartment, underlining their extreme modularity [1]. In addition, transient and low-affinity PPIs are central for shaping interactome identity *in vivo*. Therefore, capturing this type of PPIs has become a technological challenge for understanding protein function in normal or pathological condition [2].

The conventional technique to identify endogenous interactomes of a protein of interest (POI) is affinity purification (AP) with a specific antibody and the identification of interacting proteins by liquid chromatography followed by mass spectrometry (LC/MS). However, AP-based approaches have a bias towards direct, high affinity and stable PPIs [3]. Due to this limitation, the recent development of several proximity-dependent labeling (PL) methods in living cells partially addressed the difficulty to capture low affinity and transient PPIs established by a POI. These methods take advantage of promiscuous enzymes fused to the POI that can label proximal endogenous proteins (within a radius of approximately 10 nanometers), including transient and weak partners. Although different types of labeling reactions have been described, the most widespread approaches rely on the covalent binding of the small biotin molecule, allowing single-step streptavidin purification before subsequent MS analysis of labelled proteins [3]. One of the last generation and most commonly used Biotin-based proximity labeling enzymes is the TurboID, which is a directed-evolution variant of the original BioID, with less toxicity, smaller size and faster labeling activity [4]. In addition, split forms of TurboID (split-TurboID) have been developed and used for contact-dependent labeling in cells. This conditional proteomics method has been used to probe the proteomic composition in a spatiality-specific subcellular compartment [5] or cell surface environment [6,7] and to capture SUMO-dependent interactions [8]. However, the activity of the reconstituted TurboID is relatively low compared to the full length/uncut form. Consequently, it requires long incubation times with the biotin (24 hours), which forbids having access to interactome dynamics. On the other hand, biotin ligases do not allow observing PPIs in a native cellular environment.

In this work, we develop a methodology called Bi-nano-ID (**bi**color bimolecular fluorescent complementation-directed **nano**body coupled to proximity **id**entification enzyme).

68 This method aims at specifically characterizing endogenous interactomes of a specific dimeric
69 bait protein complex and visualizing each novel interaction simultaneously with the two bait
70 proteins in living cells.

71 As a proof of concept, Bi-nano-ID was established by using TAZ (WWTR1) associated
72 to two different cofactors. TAZ is a key player in the Hippo signaling pathway with a well-
73 known nucleocytoplasmic shuttling property in cells [9]. When the Hippo signaling is on,
74 upstream kinases phosphorylate TAZ, leading to its retention in the cytoplasm and interaction
75 with 14-3-3 proteins. Cytoplasmic TAZ/14-3-3 complexes promote proliferation and the
76 differentiation of different tissue types [10]. Upon Hippo signaling inactivation, TAZ
77 translocates into the nucleus and interacts with TEAD proteins, resulting in the expression of a
78 battery of target genes. TAZ/TEAD complexes are required for the differentiation of
79 osteoblasts and other cell types [11,12]. Aiming to verify the applicability of Bi-nano-ID, we
80 mapped the interactome of TAZ associated with either the long isoform epsilon of 14-3-3 (14-
81 3-3e) or the isoform 2 of TEAD (TEAD2) in human HEK293T cells. We further validated the
82 novel role of protease inhibitors in forming cooperative trimeric complexes with TAZ and 14-
83 3-3e complexes and promoting their proliferative activity in mesenchymal stem cells.

84 Overall, our work demonstrates that Bi-nano-ID is a sensitive and specific method for
85 deciphering interactomes of specific binary protein complexes in living cells.

86

87 **Results**

88 **Capturing the generic interactome of TAZ in living HEK293T cells**

89 In order to get a global picture of the TAZ interactome in HEK293T cells, as well as establishing
90 experimental parameters for LC/MS analysis of affinity-purified biotinylated proteins, we first generated
91 a TAZ-TurboID fusion construct under the control of a doxycycline (dox)-inducible promoter (see
92 Material and Methods). We also performed RNA-seq experiments, which showed that our HEK293T
93 cells express very low levels of endogenous TAZ and TEAD messengers, but did express several 14-3-3
94 isoforms (Table S1). Therefore, we concluded that the expression of TAZ-TurboID in HEK293T cells
95 will allow capturing interactions that could be associated with TAZ/14-3-3 complexes. In any case, we
96 defined all interactions that will be captured with TAZ-TurboID as "generic", since they represent all
97 possible interactions of TAZ without considering their dependency towards a specific TAZ-
98 associated cofactor (Fig. 1A).

99 The expression and activity of TAZ-TurboID was first verified by immunostaining
100 (Fig. 1B) and western blot (WB, Fig. 1C). These experiments validated the strong and specific
101 biotinylation activity of TAZ-TurboID when compared to the TurboID enzyme alone (Fig. 1B-

102 C and S1). We next performed cell protein extracts for LC/MS analysis with three biological
103 replicates of TAZ-TurboID and TurboID (see also Materials and Methods).
104 LC/MS analysis led to the identification of 243 proteins (Table S2), and we compared
105 this list to the list of previously known physical interactors of TAZ in the literature
106 (https://thebiogrid.org/117434/summary/homo-sapiens/wwtr1.html). 66 interactions were
107 common to the two lists, and one of the most enriched GO terms for these 66 known interactors
108 relates to the Hippo signaling pathway (Fig. 1D, S1 and Table S2). Interestingly, biological
109 functions associated with the hippo signaling pathway were not find in the remaining 275
110 known interactions, but were also enriched when considering the newly identified 177
111 interactions (Fig. 1D, S1 and Table S2). This analysis showed that our tools allowed the
112 capture of novel relevant candidate TAZ-interacting partners.
113 We next selected 6 known and 6 novel TAZ interactors for performing individual
114 Bimolecular Fluorescence Complementation (BiFC) in live HEK293T cells (see Materials and
115 Methods). BiFC relies on the property of monomeric fluorescent proteins to be reconstituted
116 upon complementation when the two sub-fragments are closed enough in space (10 nm, [13]).
117 It allows assessing whether two candidate proteins are part of the same protein complex with a
118 simple readout (apparition of a fluorescent signal upon excitation, Fig. 1E-E'). BiFC confirmed
119 that all tested candidates could interact with TAZ. Interaction profiles were diverse although a
120 majority were located in the cytoplasm (Fig. 1F and S1).
121 Overall, results obtained with TAZ-TurboID confirmed that the cell expression and
122 affinity purification systems were appropriate for further development of Bi-nano-ID in order
123 to capture specific interactions of TAZ/14-3-3e and TAZ/TEAD2 complexes.
124
125 **Establishing Bi-nano-ID experimental parameters in HEK293T cells**
126 Bi-nano-ID is based on an anti-GFP nanobody coupled to the TurboID enzyme on the one side,
127 and BiFC on the other side (Fig. 2A). More particularly, the nanobody (named conditionally
128 stable (cs) GFP-binding peptide, csGBP) has been engineered to be unstable when not bound
129 to its epitope, allowing getting a better signal-to-noise ratio, and was originally described in
130 the context of BiFC resulting from the complementation between the N-terminal (0-155:
131 VN155) and C-terminal (156-239: VC) fragment of Venus (a derivative of the yellow
132 fluorescent protein YFP, [14]). The same GFP nanobody, without conditionally unstable
133 mutations, has also previously been used to capture interactions of Venus-based BiFC
134 complexes by immunoprecipitation [15].

135 In this work, we aimed at testing the efficacy and specificity of the csGBP nanobody in
136 the context of a complementation system that allows performing bicolor BiFC. This
137 complementation system has been developed to visualize two different PPIs simultaneously,
138 and could serve for the subsequent validation of novel interactions of the dimeric bait protein
139 complex in living cells (Fig. 2B). Bicolor BiFC relies on the property of the N-terminal
140 fragment of YFP (yellow fluorescent protein) to complement with the C-terminal fragment of
141 the blue fluorescent protein ECFP (enhanced cyan fluorescent protein), producing a yellow-
142 like fluorescent signal [16,17]. Two different splice sites in the N-terminal fragment of YFP
143 (at the position 155 or 173) can complement with the C-terminal fragment of ECFP (156-239),
144 with the 1-173 N-terminal fragment described to produce stronger fluorescent signals than the
145 1-155 N-terminal fragment [16]. Here, we tested the two complementation sites by using the
146 Venus and Cerulean fluorescent proteins, which display faster maturation time and higher
147 fluorescence brightness than YFP and ECFP, respectively (Fig. S2 and [18,19]). Practically,
148 TAZ was fused to the 155- or 173 N-terminal fragment of Venus (making VN155-TAZ and
149 VN173-TAZ constructs), and the 14-3-3e and TEAD2 cofactors were fused to the 156-239 C-
150 terminal fragment of Cerulean (making CC-14-3-3e and CC-TEAD2 constructs). All
151 constructs were under the same dox-inducible promoter and BiFC was analyzed in living
152 HEK293T cells. Results showed that BiFC obtained with the VN155 fragment was extremely
153 weak when compared to BiFC obtained with VN173, underlining that VN155 could not
154 complement efficiently with the CC fragment in both TAZ/14-3-3e and TAZ/TEAD2
155 complexes (Fig. S2). BiFC with VN173-TAZ also validated the correct cytoplasmic or nuclear
156 localization of TAZ/14-3-3e and TAZ/TEAD2 complexes in live HEK293T cells, respectively
157 (Fig. S2). Collectively, these experiments confirmed that the VN155 fragment was not best
158 appropriate for doing bicolor BiFC and we thus decided to establish Bi-nano-ID by using the
159 VN173 fragment.
160 Compared to the previous systems that were based on immunoprecipitation and
161 constitutive expression [15,20], the csGBP nanobody was here under the control of a dox-
162 inducible promoter and fused to the TurboID PL enzyme (see Materials and Methods). These
163 modifications allow getting a more specific and sensitive capture of protein partners.
164 The specificity of the csGBP-TurboID nanobody was first evaluated by
165 immunofluorescence. BiFC constructs were co-transfected with the nanobody tool and biotin
166 was added to visualize both BiFC and biotinylation (revealed by using Streptavidin Alexa-555)
167 in the same cells (see Materials and Methods). Confocal analyses confirmed that BiFC and
168 biotinylation signals colocalized in the case of TAZ/14-3-3e and TAZ/TEAD2 complexes (Fig.

169 2C-D). In contrast, no biotinylation could be revealed when expressing the csGBP-TurboID
170 nanobody alone or together with the individual VN173-TAZ, CC-14-3-3e or CC-TEAD2
171 construct, demonstrating that the biotinylating activity was fully dependent on the binding of
172 the nanobody to BiFC complexes (Fig. S3). Biotinylation signals were also extremely weak in
173 the case of BiFC complexes with VN155-TAZ, underlining that the binding affinity of the
174 nanobody was dependent on the complementation efficiency between the N- and C-terminal
175 fragments (Fig. S2).
176 Next, we tested the specificity of our tools by doing WB upon affinity purification (AP)
177 with streptavidin-coupled beads. We used the same BiFC and control conditions as described
178 for the immunostaining. Proteins were extracted, purified and revealed after different
179 timepoints of incubation with the biotin to select the best experimental condition for having
180 strong BiFC-specific biotinylation signals with a good signal-to-noise ratio. All quantifications
181 were performed by normalizing the AP over the input and the correct expression of each
182 construct was also validated by using an anti-GFP recognizing the VN and CC fragments
183 (Fig.S4). Results showed non-specific biotinylation activity of the nanobody in the absence of
184 any BiFC constructs (first four lanes in Fig. 2E). Importantly, signals were strongly enriched
185 in the presence of BiFC complexes and quantifications showed that the best incubation time
186 was 180 min, with no stronger BiFC-specific biotinylation signals at 240 min (Fig. 2E-E' and
187 S4). The specificity of the nanobody was also more precisely quantified by considering each
188 single construct. This analysis showed negligeable biotinylation activity in the case of CC-14-
189 3-3e and CC-TEAD2 constructs (Fig. 2E and S4). In contrast, some signal could be observed
190 with VN-TAZ alone, indicating that the csGBP-TurboID nanobody was weakly recognizing
191 the VN173 fragment (Fig. 2E and S4). In conclusion, these experiments established the
192 experimental conditions for purifying BiFC-specific interactomes with the csGBP-TurboID
193 nanobody tool. Because of the weak recognition of the VN173 fragment by the nanobody, we
194 also considered VN-TAZ as an additional filtering control for the analysis of BiFC-specific
195 MS data (see below).
196
197 **Using Bi-nano-ID to capture specific interactomes of TAZ/14-3-3e and TAZ/TEAD2**
198 **complexes in living HEK293T cells**
199 Mass spectrometry analysis was performed by using the streptavidin affinity purified fraction
200 of protein extracts from HEK293T cells in the different control and BiFC conditions. Control
201 conditions consisted in the expression of the nanobody alone (to discriminate for the general
202 background of the TurboID enzyme, referred to as csGBP-TurboID), and to the co-expression

203 of csGBP-TurboID with VN-TAZ (to discriminate for the weak affinity of the nanobody to the
204 VN173 fragment). These two control conditions were used to filter interactions obtained in the
205 two BiFC conditions (csGBP-TurboID co-expressed with VN-TAZ and CC-14-3-3e or with
206 VN-TAZ and CC-TEAD2, Fig. S5).

207 Results showed a good reproducibility between the three biological replicates in each
208 experimental condition (Table S3), and we considered interactions that were present in two or
209 three replicates for subsequent analyses. Interactions with BiFC complexes were filtered with
210 the interactions obtained in the two control conditions, which led to the identification of 96 and
211 42 candidate interactions for TAZ/14-3-3e and TAZ/TEAD2 complexes, respectively
212 (Materials and Methods, Table S3 and Fig. S5).

213 To better discriminate for TAZ/14-3-3e- and TAZ/TEAD2-dependent interactions, we
214 compared the two BiFC interactomes with the interactome obtained with TAZ-TurboID. This
215 analysis revealed 50 and 30 interactions that were specifically found with TAZ/14-3-3e and
216 TAZ/TEAD2 BiFC complexes, respectively (Fig. 3A and S6). The finding of 50 interactions
217 specific of the TAZ/14-3-3e BiFC complex underlines that endogenous 14-3-3e did not hid all
218 specific binary complex interactions (although half of the 96 interactions of the TAZ/14-3-3e
219 BiFC complex were also captured with TAZ-TurboID).

220 Finally, since the goal of Bi-nano-ID was to capture specific interactions of the
221 cytoplasmic TAZ/14-3-3e versus nuclear TAZ/TEAD2 complexes, we compared their
222 respective interactomes. This last analysis revealed 32 interactions that were specific of
223 TAZ/14-3-3 and 12 interactions that were specific of TAZ/TEAD2 (Fig. 3A and S6). Thus,
224 Bi-nano-ID was successful in capturing BiFC-specific interactomes.

225 In order to better know the functions associated with the common and specific TAZ-
226 related interactomes, we performed a GO-term enrichment analysis for each interactome (see
227 Materials and Methods and Table S3). "Hippo signaling pathway" was strongly enriched in
228 TAZ/14-3-3e and TAZ/TEAD2 interactomes (in addition to the TAZ-TurboID interactome),
229 emphasizing that our tools led to the capture of functionally relevant interactions (Fig. 3B and
230 S7). Interestingly, functions related to mRNA stability and catabolic processes were also
231 enriched in the three interactomes, suggesting that they also represent a major and generic
232 molecular facet of TAZ (Fig. 3B and S7). Several GO terms were specifically associated with
233 TAZ/14-3-3e or TAZ/TEAD2 interactome. Importantly, some of these specific functions were
234 consistent with the known activity of 14-3-3 and TEAD proteins on YAP/TAZ effectors (such
235 as nuclear export and stem cell division for TAZ/14-3_3e or nuclear import import and
236 transcription for TAZ/TEAD2, Fig. 3B). Other specific functions (like "negative regulation of

237 adipose tissue development" and "circadian rhythm" for TAZ/14-3-3e, or "keratinocyte
238 development" and "odontoblast differentiation" for TAZ/TEAD2) have been described in the
239 literature with YAP/TAZ (see for example [21–24]). These observations underline that Bi-
240 nano-ID was efficient for capturing novel interactions that could be involved in known specific
241 TAZ/14-3-3e and TAZ/TEAD2 functions. Finally, not all the generic TAZ functions were
242 captured with the TAZ/14-3-3e and TAZ/TEAD2 interactomes (like oocyte maturation or
243 mitophagy regulation, Fig. S7), suggesting that these TAZ functions could rely on other 14-3-
244 3/TEAD-independent partnerships.
245
246 **SERPINB4 potentiates the proliferative activity of TAZ and 14-3-3e in HS27A**
247 **mesenchymal stem cells**
248 YAP/TAZ regulators have context-dependent roles in stem cells, either driving self-renewal or
249 differentiation depending on the identity of the stem cell [25,26]. These differential activities
250 are also linked to the cytoplasmic or nuclear localization, therefore to the association with
251 cytoplasmic (including 14-3-3) or nuclear (including TEAD) cofactors. Here, we wondered
252 whether some specific TAZ/14-3-3e or TAZ/TEAD2 interactions captured with Bi-nano-ID
253 could be functionally validated in a stem cell context. To this end, we considered the HS27A
254 bone marrow mesenchymal stromal cell line that can be induced into different cell types
255 depending on the cell culture medium [27,28]. Given that a common enriched GO term for
256 TAZ/14-3-3e and TAZ/TEAD2 complexes was related to the "positive regulation of osteoblast
257 differentiation" (Fig. 3B and Table S3), we decided to cultivate HS27A cells in an osteoblast-
258 differentiation medium. The differentiation into osteoblast was confirmed with Alizarin red
259 staining (see Materials and Methods and Fig. 4A). We hypothesized that cofactors working in
260 concert with TAZ/14-3-3e or TAZ/TEAD2 complexes could potentially display distinct
261 expression profiles depending on the mesenchymal-like/undifferentiated or osteoblast-
262 like/differentiated state of HS27A cells. In order to identify such candidate cofactors, we
263 performed RNA-seq experiments of HS27A cells at day 1 (proliferation state) and at day 15
264 (osteoblast differentiation state). RNA-seq data showed several genes that were strongly up- or
265 down-regulated when comparing the proliferative and differentiated state of HS27A cells (Fig.
266 4B and Table S4). Unexpectedly, neither *TAZ*, nor *TEAD* or *14-3-3* genes showed a significant
267 differential expression level between the undifferentiated and differentiated cell state (Table
268 S3). This observation suggests that their role could depend on post-transcriptional regulatory
269 process, such as the regulation of the nuclear shuttling. Nevertheless, although a number of the
270 genes displaying a differential expression profile could correspond to downstream effectors of

271 TAZ/14-3-3e and TAZ/TEAD2 complexes, we crossed these lists of differentially expressed
272 genes to our lists of specific candidate cofactors captured with Bi-nano-ID. This analysis led
273 to the identification of *SERPINB3* and *SERPINB4.* Interestingly, these two genes were among
274 the most downregulated genes during the differentiation process, and the corresponding
275 proteins were specifically captured with TAZ/14-3-3e (LC/MS analysis could not discriminate
276 between SERPINB3 and B4, which are 100% identical at the protein sequence level, Fig. 3B
277 and S8). SERPINB4 has previously been described to promote squamous cell carcinomas [29]
278 and was recently associated with psoriasis severity that is characterized by epidermal
279 hyperproliferation and infiltration of inflammatory cells [30]. Moreover, the analysis of the
280 known interactome of SERPINB4 revealed two other interaction partners that were specifically
281 captured with TAZ/14-3-3e: S100A8 and S100A9 (Fig. 3B-C and 4C). These two proteins have
282 been described to be part of a common circuit with the hippo signaling and promote the
283 proliferation and colony formation of breast cancer cells [31]. Finally, "stem cell division" was
284 also among the most enriched GO terms specific of the TAZ/14-3-3e interactome (Fig. 3B and
285 Table S3). Altogether, these observations suggest that SERPINB3 and B4 could play a role for
286 the proliferation of HS27A cells, making them strong candidates to test in the context of
287 TAZ/14-3-3e proliferative activity.
288 To test this hypothesis, we generated two different siRNAs targeting *TAZ*, *14-3-3e* or
289 *SERPINB3* and *B4*. The specificity of each siRNA was individually tested in HS27A cells (Fig.
290 S8 and Materials and Methods) and we next assessed their effect on HS27A cells proliferation,
291 either alone or in various heterologous combinations. Results showed that the individual
292 targeting of *TAZ, SERPINB3/B4* or *14-3-3e* affected the proliferation rate of HS27A cells at
293 35h post transfection, and this effect tended to fade over time (at 50h, which could be explained
294 by siRNA dilution over cell generations; Fig. 4D). Importantly, combining siRNAs against
295 *SERPINB3/B4* and *TAZ* or *SERPINB3/B4* and *14-3-3* already impacted proliferation at 25h
296 post-transfection, and further decreased HS27A proliferation rate when compared to individual
297 siRNAs (Fig. 4D). These combinatorial effects were similar to the one observed when
298 combining *TAZ* and *14-3-3* siRNAs and were more persistent over time when compared to
299 individual siRNAs (Fig. 4D). These results show that SERPINB3 and B4 are required for the
300 proliferation of HS27A cells and act in concert with TAZ and 14-3-3. Moreover, this effect
301 was independent of epistatic relationships given that the knock-down of *SERPINB3* and *B4* had
302 no effect on *TAZ* or *14-3-3e* expression (Fig. S8). Thus, *SERPINB3* and *B4* could have a
303 redundant role for promoting the proliferative activity of TAZ/14-3-3e complexes in HS27A

304 cells. We hypothesize that this cooperative activity could result from the formation of specific
305 trimeric protein complexes.
306
307 **Specific interaction interfaces allow the formation of trimeric TAZ/14-3-3e/SERPINB4**
308 **complexes**
309 The ability of SERPINB3-B4 to interact with TAZ and 14-3-3e was tested by performing
310 bicolor BiFC. We used *SERPINB4* as a cDNA template for generating the fusion CC-
311 SERPINB4 construct, knowing that conclusions reached with this construct will also apply for
312 SERPINB3. CC-SERPINB4 was expressed with VN-TAZ and CN-14-3-3e to simultaneously
313 visualize its interaction with either TAZ or 14-3-3e in the same living cell context (Fig. 5A).
314 Confocal analysis showed overlapping Venus and Cerulean signals with a diffuse pattern and
315 few enrichment dots in the cytoplasm (Fig. 5A'-A"). The observation of superposable Venus
316 and Cerulean BiFC signals indicates that TAZ-SERPINB4 and SERPINB4-14-3-3e
317 interactions occur at the same locations within the cell, strongly suggesting that the three
318 proteins could be part of a same trimeric complex.
319 To assess the role of 14-3-3e for TAZ-SERPINB4 interaction, we performed BiFC
320 between VN-TAZ and CC-SERPINB4 when affecting simultaneously endogenous *14-3-3e*
321 expression in HEK293T cells (around 60% loss was obtained upon siRNA transfection, Fig.
322 5B and S8). Under this condition, BiFC signals were strongly diminished (around 50% loss,
323 Fig. 5B'-B'"), underlining that endogenous 14-3-3e is promoting TAZ-SERPINB4 interaction.
324 Given that HEK293T cells express low levels of endogenous *TAZ*, we also performed
325 the complementary experiment by looking at BiFC between VN-14-3-3e and CC-SERPINB4
326 when over-expressing HA-tagged TAZ (Fig. 5C). Under this condition, BiFC signals were
327 increased around 7 folds, demonstrating that TAZ could also promote the interaction between
328 14-3-3e and SERPINB4 (Fig. 5C'-C").
329 Altogether, these experiments established that binary interactions between SERPINB4 and
330 TAZ or SERPINB4 and 14-3-3e were increased in the presence of the third partner, strongly
331 suggesting that TAZ, 14-3-3e and SERPINB4 could form a cooperative trimeric protein
332 complex.
333 In order to better understand how the trimeric TAZ/14-3-3e/SERPINB4 complex could
334 be formed, we used the artificial intelligence platform AlphaFold for structure prediction
335 (https://alphafold.ebi.ac.uk/ and [32]) and ENDscript for extracting and having a
336 comprehensive visualization of all contacts between the three partners [33]. Interestingly,
337 AlphaFold predicted several structured complexes with good confidences score (between 600

338 and 700). More particularly, the top ranked model showed that a C-terminal disordered region
339 of TAZ was falling between the interface of interaction with 14-3-3e and SERPINB4 (Fig. S9).
340 This disordered region of TAZ contains a predicted short linear interaction motif (SLIM) that
341 could be recognized by LATS kinases in the cytosol ([34–36] and Fig. S9). More specifically,
342 the Glu309 of this SLiM interacts with two Lys residues of SERPINB4 at position 189 and
343 237, and no other contacts are predicted between TAZ and SERPINB4 (Fig. S9). In contrast,
344 several residues at the N- and C-terminus of 14-3-3e are predicted to contact TAZ (Fig. S9). In
345 particular, the residue D234 interacts with the residue R308 of TAZ (Fig. S9), underlining that
346 the C-terminal SLIM of TAZ is a central node for making strong interactions with both
347 SERPINB4 and 14-3-3e.
348 To experimentally validate the predictive interaction interface of TAZ with SERPINB4,
349 we mutated the residue Glu309 into an Alanine residue (construct $TAZ^{E309A}$), anticipating that
350 this mutation could affect TAZ/SERPINB4 interaction specifically in the context of
351 TAZ/SERPINB4/14-3-3e trimeric complex. Indeed, interaction interfaces are all predicted to
352 be different when comparing the trimeric complex to the different dimeric complexes (Fig.
353 S10-12). In particular, the residue Glu309 of TAZ is not predicted to contact any SERPINB4
354 residues in the dimeric TAZ/SERPINB4 complex (Fig. S10). These predictions underscore that
355 binary interactions could be completely remodeled in the presence of the third partner.
356 The correct expression and localization of $TAZ^{E309A}$ was verified (Fig. S9) and the effect of the
357 TAZ punctual mutation was analyzed by doing bicolor BiFC to simultaneously analyze the
358 interaction of SERPINB4 with either $TAZ^{E309A}$ or 14-3-3e (Fig. 6A). Results showed 80% loss
359 of BiFC between SERPINB4 and $TAZ^{E309A}$, thus confirming that the residue E309 of TAZ was
360 central for recruiting SERPINB4 in the context of the trimeric complex (Fig. 6A'-A"). The
361 inability of $TAZ^{E309A}$ to interact with SERPINB4 was also indirectly demonstrated by the
362 absence of any promoting effect of HA-$TAZ^{E309A}$ when over-expressed with VN-14-3-3e and
363 CC-SERPINB4 (Fig. 6B-B"), indicating that HA-$TAZ^{E309A}$ lost most of its ability to form a
364 trimeric complex with SERPINB4 and 14-3-3e.
365 Surprisingly, bi-colour BiFC in the context of VN-$TAZ^{E309A}$ also showed a strong
366 decrease (around 50%) of signal between CN-14-3-3e and CC-SERPINB4 (Fig. 6A'-A").
367 Thus, the loss of interaction between $TAZ^{E309A}$ and SERPINB4 also affected the interaction
368 between SERPINB4 and 14-3-3e, underlining that the interaction interfaces between
369 SERPINB4 with 14-3-3e were remodeled when TAZ was not interacting with SERPINB4.
370 To further confirm that interaction interfaces are different when considering the trimeric and
371 dimeric complexes, we analyzed the effect of the E309A mutation of TAZ in the absence of

372 14-3-3e. To this end, we repeated the analysis of BiFC between VN-TAZ$^{E309A}$ with CC-
373 SERPINB4, in wild type condition or by simultaneously expressing *14-3-3e* siRNA (Fig. 6C).
374 First, we observed BiFC despite the presence of endogenous *14-3-3e* in wild type condition
375 (Fig. 6C'). This observation confirmed that VN-TAZ$^{E309A}$/CC-SERPINB4 dimeric complexes
376 could be formed in excess with regard to endogenous 14-3-3e. Importantly, depleting
377 endogenous *14-3-3e* did not affect the BiFC signals, demonstrating that TAZ$^{E309A}$/SERPINB4
378 complexes were formed through distinct and 14-3-3e-independent interaction interfaces as
379 compared to TAZ-SERPINB4 interactions established in the context of trimeric
380 TAZ/SERPINB4/14-3-3 BiFC complexes (Fig. 6C'-C").
381 Collectively, these experiments confirmed that the E309 residue of TAZ is used for
382 interacting with SERPINB4 in the specific context of the trimeric association with 14-3-3e. In
383 addition, the interaction of SERPINB4 with the E309 residue of TAZ allows SERPINB4 to
384 interact with 14-3-3e, thus showing the mutual dependency of each partner to form a
385 cooperative trimeric protein complex.
386
387 **Discussion**
388 In this study, we developed and validated Bi-nano-ID, a novel method that combines BiFC
389 with proximity-dependent biotinylation, to investigate binary protein interactions and their
390 associated interactomes in living cells. By using TAZ/14-3-3e and TAZ/TEAD2 interactions
391 as a proof-of-concept, we demonstrated the efficacy of Bi-nano-ID in capturing and
392 characterizing these interactions within their specific cellular compartments.
393
394 **Advantages of Bi-nano-ID over other experimental approaches**
395 To date, the unique alternative methodologies to capture interactomes of dimeric complexes
396 rely on split-BioID and split-TurboID enzymes, which can be reconstituted upon spatial
397 proximity. These approaches have been used to identify interactomes of different dimeric
398 protein complexes and to monitor [8,37,38] or capture interactions in specific cellular
399 compartments [5]. However, these systems have to deal with the strong auto-affinity between
400 the split TurboID fragments and require long biotin incubation times (minimum 8 hours) due
401 to the decreased activity of the reconstituted TurboID. In contrast, Bi-nano-ID integrates BiFC,
402 which is well established for providing a specific readout of many different types of PPIs. In
403 addition, the use of a BiFC-recognyzing nanobody allows the robust and rapid biotinylation
404 capabilities of full length TurboID. This combination enhances the specificity and sensitivity
405 for detecting protein interactions and their proximate interactomes within defined cellular

406 localization. Finally, by using fragments compatible for bi-color BiFC, Bi-nano-ID allows to
407 rapidly validate candidate proteins of the interactome together with the bait dimeric complex
408 in living cells.
409
410 **Bi-nano-ID identified distinct interaction partners for TAZ/14-3-3e and TAZ/TEAD2**
411 **complexes**
412 Interactions between TAZ and 14-3-3e or TAZ and TEAD2 were visualized using BiFC,
413 showing distinct cytoplasmic and nuclear fluorescence patterns respectively, and confirming
414 their subcellular localization as influenced by the Hippo signaling pathway. This initial
415 validation set the foundation for integrating the csGBP nanobody fused with the TurboID
416 enzyme, which led to the biotinylation of proteins in proximity to the BiFC complexes. The
417 subsequent biotinylation was specific and colocalized with the BiFC signals, as revealed by
418 immunofluorescence and Western blot analyses, indicating the precision and reliability of Bi-
419 nano-ID in live-cell contexts.
420 Due to the weak recognition of the VN173 fragment by the csGBP nanobody, we also
421 tested our tools when using VN155-TAZ, which was not recognized by the nanobody in
422 previous work [15]. These assays showed that BiFC was weak and not exploitable with 14-3-
423 3e or TEAD2 fused to the CC fragment. Consequently, biotinylation was also less efficient.
424 We concluded that VN155 was much less appropriate than VN173 in our bi-color
425 complementation strategy. In addition, using VN173-TAZ alone as a negative control was
426 efficient for discriminating the background resulting from the weak affinity of the csGBP
427 nanobody for the VN173 fragment in the mass spectrometry analysis.
428 Our work identified a substantial number of proteins in proximity to TAZ/14-3-3e and
429 TAZ/TEAD2 complexes. The stringent filtering process ensured high specificity, leading to
430 the identification of 96 candidates for TAZ/14-3-3e and 42 candidates for TAZ/TEAD2.
431 Further refinement excluded proteins identified in proximity to TAZ alone, isolating 50 unique
432 TAZ/14-3-3e interactors and 30 unique TAZ/TEAD2 interactors. Gene ontology enrichment
433 analyses revealed that TAZ-TurboID, TAZ/14-3-3e and TAZ-TEAD2 interactors all
434 predominantly participate in Hippo pathway regulation, highlighting that our approach was
435 successful for revealing novel interactions that could modulate TAZ function. Importantly,
436 TAZ/14-3-3e and TAZ/TEAD2 interactomes displayed clear distinct GO term enrichments,
437 allowing assigning specific functions of TAZ to the association with either 14-3-3e or TEAD2
438 cofactors. Collectively, these results demonstrate the suitability of Bi-nano-ID for capturing

439 and distinguishing interactomes of a bait protein associated with a different cofactor in two
440 different cellular compartments.
441
442 **Molecular insights into TAZ/14-3-3e/SERPINB4 complex formation and its biological**
443 **implications**
444 Our detailed molecular dissection using bicolor BiFC and mutagenesis identified a critical
445 interaction interface for both 14-3-3e and SERPINB4 within the TAZ protein. More
446 particularly, this region encompasses residues 307-315 and is predicted to be phosphorylated
447 by LATs kinases, therefore under dynamic regulation depending on the activation of the Hippo
448 pathway. Importantly, mutating the single Glu309 residue of TAZ predicted to form
449 electrostatic interactions with two Lys residues of SERPINB4 was sufficient to abolish all
450 cooperative interactions involved for the trimeric complex assembly. Interestingly, the
451 Glu309Ala mutation was able to also affect the interaction between 14-3-3e and SERPINB4
452 but only in the context of the trimeric complex, highlighting that 14-3-3e and SERPINB4 have
453 TAZ-dependent and TAZ-independent modes of interaction (Fig. 7). We suggest that the TAZ-
454 dependent mode of interaction, therefore interaction in the context of trimeric TAZ/14-3-
455 3e/SERPINB4 complexes, could be more stable and potentiate the proliferative activity of
456 TAZ/14-3-3 complexes. This hypothesis results from our assays in human bone marrow
457 stromal cells (HS27A) but could potentially apply more generally in cell progression,
458 proliferation and metastasis for cancer biology and tissue regeneration. In this context, the
459 identification of the most relevant interaction interface used in the trimeric and not the dimeric
460 complex could have strong incidence for future therapeutic development.
461 In conclusion, our work highlights the importance of considering interactomes of dimeric
462 protein complexes over single bait proteins, and the relevance of Bi-nano-ID in this
463 perspective.
464
465 **Materials and Methods**
466 **Cell culture**
467 HEK293T cells were purchased from the European Collection of Authenticated Cell Cultures
468 (ECACC) through the biological resource center CelluloNet (AniRA platform of the
469 UAR3444, Lyon, France). Human bone marrow stromal cells (HS27A) were a gift from the
470 team of Dr. Véronique Maguer-Satta (CRCL). HEK-293T cells were cultured as a monolayer
471 in Dulbecco's modified Eagles medium (DMEM-GlutaMAX-I, Gibco by Life Technologies)
472 supplemented with 10% (*v/v*) heat-inactivated fetal bovine serum (FBS) (Gibco by Life

473 Technologies), 1% (*v/v*) Penicillin-Streptomycin (5,000U penicillin and 5mg
474 streptomycin/mL, Gibco), and 5 ml of 100 mM sodium pyruvate (Gibco by Life Technologies)
475 incubating at 37°C, in an atmosphere of 5 % $CO_2$. HS27A cells were cultured in RPMI 1640
476 (Gibco by Life Technologies) supplemented with 10% (*v/v*) heat-inactivated fetal bovine serum
477 (FBS) (Gibco by Life Technologies) and 1% (*v/v*) Penicillin-Streptomycin (5,000U penicillin
478 and 5mg streptomycin/mL, Gibco) incubating at 37°C, in an atmosphere of 5 % $CO_2$.
479
480 **Cloning**
481 Plasmids used in this study were cloned either by gateway cloning or conventional restriction
482 digestion into pLIX _403 vector (a gift from David Root; Addgene plasmid #
483 41395; http://n2t.net/addgene:41395, RRID: Addgene_41395). All constructs are placed under
484 the same tet-off dox-inducible promoter. All constructs were sequenced (Genewiz company,
485 Germany) before using. Oligonucleotides used for the cloning are listed (Table S5).
486
487 **Fluorescent immunostaining**
488 $50.10^5$ HEK-293T cells were seeded on glass coverslips in 24-well plate for 18-24 hours to
489 about 80% confluency, then transiently transfected with 250 ng of each plasmid using
490 jetPRIME (Polyplus, Ref 114-15) and following manufacturer's instructions in the presence of
491 doxycycline (dox, 100 ng/ml). After 14h of dox induction, cells were washed with PBS and
492 replaced by fresh complete media without dox for 6h at 37°C. Cells were then cultured in 50
493 µM Biotin for 3h at 37°C under 5% $CO_2$. Cells were then washed twice with 1X PBS and fixed
494 with 4% (*v/v*) paraformaldehyde at 4°C for 15 min. In between each step, cells were washed
495 with 1X PBS. Cells were permeabilized with 0,1% Triton for 10 min followed by a blocking
496 step in 2% (*w/v*) BSA for 1h at RT. Cells were then incubated with primary antibody (Rabbit-
497 anti-GFP A11122 Invitrogen at 1/1000) in PBS supplemented with 2% (w/v) BSA for 3 hr at
498 RT. Next, samples were incubated with anti-rabbit-Alexa Fluor 488 and Alexa Fluor 555-
499 Streptavidin to reveal biotinylated proteins, in PBS supplemented with 2% (w/v) BSA for 1 hr
500 at RT. Finally, cell-coated coverslips were mounted in VECTASHIELD antifade mounting
501 medium with DAPI (VECTOR, Cat No. LS-J1033-10) and imaged by confocal microscopy
502 (Zeiss LSM780).
503
504 **Western blots**
505 Cells were cultured in Biotin (50 µM) at 37°C under 5% $CO_2$ at several incubation times (10
506 min, 90min, 180min, and 240min). Cells were washed twice with 10 ml ice-cold DPBS,

507 harvested by scraping, pelleted by centrifugation at 1,400 r.p.m. for 3 min, and either processed
508 immediately or stored at -80°C before further analysis.
509 The protocol of TurboID labeling (with TurboID-HA or TAZ-TurboID-HA constructs) is
510 similar to the approach followed for Bi-nano-ID labeling, except that cells were incubated with
511 biotin 50 µM for 10 min.
512 Collected cell pellets for both Western blotting (WB) and proteomic analysis were resuspended
513 in ice-cold RIPA/1%SDS-cell lysis buffer (50mM Tris pH8, 150mM NaCl, 0.5% sodium
514 deoxycholate, 1% NP40/IGEPAL) (volume ratio between cell pellet: buffer = 1:3) and
515 incubated on ice for 20-30 min, maintaining constant vortex (2-3 times). The cells were then
516 treated with Benzonase Nuclease (Sigma, E1014-25KU) for 10 to 20 min on ice or to observe
517 the solution becomes less viscous. This was subjected to spin at 14000×g at 4°C for 10 min.
518 The supernatant was then transferred to 1,5 Eppendorf tube. To test the expression of the
519 constructs, 10% of the protein extracts were kept for WB as input fraction. Proteins were
520 quantified using Pierce BCA Protein Assay (Thermofischer, A55865). Streptavidin magnetic
521 beads (Sigma, 88817) were equilibrated with two PBS washes and resuspended in RIPA buffer
522 supplemented with 1% SDS (50 mM Tris pH 8, 150 mM NaCl, 0.5% sodium deoxycholate,
523 1% NP40, 1% SDS). 1 mg of protein extracts were incubated with 40 µl of streptavidin beads
524 in a final volume of 1 ml RIPA-SDS overnight at 4°C on a rotating wheel. Beads were then
525 washed twice with SDS-Buffer (10 mM Tris.HCl, 1 mM EDTA, 1% SDS, 200 mM NaCl),
526 twice with RIPA-SDS and twice with acetonitrile buffer (20% acetonitrile in MS-grade water).
527 For WB validation, acetonitrile washing step was skipped.
528 For western blot analysis, proteins (Input and AP) were resolved on 12% SDS-PAGE, blotted
529 onto PVDF membrane (Biorad) and probed with specific antibodies after saturation. The
530 antibodies (and their dilution) used in this study were, Histone 3 (1791 Abcam, 1/10,000), GFP
531 (A11122 Life Technologies, 1/1000), and Streptavidin-HRP (SA10001 Invitogen, 1/5000).
532 Developing was performed using chemiluminescence reaction (ECL, Cytiva) with secondary
533 antibody coupled to HRP (Promega, 1/5000).
534
535 **Mass spectrometry preparation**
536 Streptavidin beads were resuspended in 14 µl of ammonium bicarbonate 50 mM and proteins
537 were subjected to reduction with 1 µl DTT (100 µM, 57°C, 45min) and alkylation with 1µl
538 iodoacetamide (500µM, RT, 45min at dark). The proteins were then digested with a mixture of
539 endoproteinase Lys-C/trypsin (ratio protein/enzyme 1/100, overnight, 37°C, 500 rpm). After a
540 cleaning step with SP3 beads, peptides were dried, suspended in Formic Acid (FA) 0.1%,

541 DMSO 2% and injected in the mass spectrometer. Samples were analyzed on a Q Exactive HF
542 mass spectrometer coupled with a nanoRSLC Ultimate 3000 system (ThermoFisher Scientific).
543 Peptides samples were loaded on a C18 Acclaim PepMap100 trap-column 300 µm ID x 5 mm,
544 5 µm, 100Å (ThermoFisher Scientific) and separated on a C18 Acclaim Pepmap100 nano-
545 column, 50 cm x 75 µm i.d, 2 µm, 100 Å (ThermoFisher Scientific) with a 60 minutes linear
546 gradient from 3% to 90% buffer B (A: 0.1% FA in $H_2O$, B: 0.1% FA in ACN). The flow rate
547 was maintained at 300 nL/min and the oven temperature was kept constant at 40°C. Peptides
548 were analysed using a DDA TOP20 HCD method: MS data were acquired in a data dependent
549 strategy (DDA) selecting the fragmentation events based on the 20 most abundant precursor
550 ions in a survey scan (350-1400 Th). Resolutions of the survey and MS/MS scans were
551 respectively set at 60,000 and 15,000 at m/z 200 Th. The Ion Target Values for the survey and
552 the MS/MS scans in the Orbitrap were set to 3E6 and 1E5 respectively and the maximum
553 injection times were set to 60 ms for both MS and MS/MS scans. Parameters for acquiring
554 HCD MS/MS spectra were as follows: collision energy = 27 and isolation window = 2 m/z.
555 The precursors with unknown charge state, charge state of 1 and 8 or greater than 8 were
556 excluded. Peptides selected for MS/MS acquisition were then placed on an exclusion list for
557 30 s using the dynamic exclusion mode to limit duplicate spectra.
558
559 **Mass spectrometry analyses**
560 Each batch of experiment included TurboID and TAZ fused to TurboID samples (Table S2),
561 and csGBP-TurboID, csGBP-TurboID with VN-TAZ, csGBP-TurboID with VN-TAZ and
562 CC-14-3-3e, csGBP-TurboID with VN-TAZ and CC-TEAD2 samples (Table S3). Each
563 condition was performed in three independent biological replicates. Raw mass spectrometry
564 data were analysed using MaxQuant free software including the Andromeda search Engine
565 [39]. Using *Homo sapiens* (Swissprot) database peptide were identified. Default parameters of
566 MaxQuant were used with the following modifications: digestion by Trypsin/P and LysC,
567 lysine biotinylation as variable modification (as well as methionine oxidation and N-terminal
568 acetylation), cytosine carbamidomethylation as fixed modification, Instrument set Orbitrap
569 (with precursor tolerance 20 ppm, MS tolerance 0.5 Da), match between runs option was
570 activated, FDR 1%, label-free quantification (LFQ) and iBAQ were calculated (Tables S2 and
571 S3). Protein enrichment was calculated using the LFQ Log2 ratio and normalized on the median
572 value (Table S2 and S3). For each ratio, distribution (90%) and corresponding standard
573 deviations (SD) were calculated to define the proteins significantly enriched (ratio > confidence
574 interval defined as median ± 2 SD). Imputation of value divided by 0 (referred to infinite) has

575 been performed for confidence intervals calculation (Table S1 and S2). Subsequently, proteins
576 significantly enriched in at least 2 replicates were considered biologically relevant considering
577 biological variability and stochasticity of the MS-process and used for further analysis (Table
578 S2 and S3). Enriched proteins from the different samples were then compared with discriminate
579 proteins enriched in proximity with csGBP-TurboID individually or in proximity with VN173-
580 TAZ alone. Details about the filtering process are detailed (Fig. S5). For TAZ generic
581 candidates, protein enrichment was calculated using the LFQ Log2 ratio of TAZ-
582 TurboID/TurboID and normalized on the median value with distribution (90%) and
583 corresponding standard deviations (SD) were calculated to define the proteins significantly
584 enriched (ratio > confidence interval defined as median ± 2 SD).
585 Raw data of MS analyses, Uniprot and contaminant databases and Maxquant files that support
586 the findings of this study will be deposited in PRIDE (https://www.ebi.ac.uk/pride/archive).
587 The mass spectrometry proteomics data will be deposited to the Center for Computational Mass
588 Spectrometry repository (University of California, San Diego) via the MassIVE tool.
589
590 **Data analysis and visualisation**
591 For proteome analysis, Perseus free software was used to generate clustering visualization
592 (PCA, [40]), based on LFQ log10 value of protein expressed after Perseus canonical filtering
593 (Reverse, Potential Contaminant, only identified by site) and replacement of missing values.
594 Functional networks of TAZ interactome were generated with STRING software [41], based
595 on 0.15 interaction score of experimental evidence and database and pathway co-occurrence.
596 Visualization of networks was built with Cytoscape free software [42]. For GO-Term
597 annotations and over-represented GO-Term related to biological process analysis was
598 performed using PANTHER [43] and represented using Prism. The selection of significant
599 GO-term was corrected by FDR<0.05, a fold enrichment higher than 10 and a raw p-
600 value>0.05. Statistical analyses were performed using one-way ANOVA (BiFC quantification,
601 siRNA effect, proliferation assay). Predictions of TAZ/1433e/SERPINB4 interaction model
602 was performed using Alphafold [32].
603
604 **BiFC and Multicolor BiFC validation**
605 For transfection, $3.10^5$ HEK293T cells were seeded on glass coverslips in 6-well plates and
606 incubated for 24h. Then, cells were transfected with jetPRIME (Ref 114-15, Polyplus
607 Transfection, France) following manufacturer's instructions. A total of 1 µg of plasmid DNA
608 (CC, VN and CC tagged proteins constructs including mcherry reporter to assess transfection

609 efficiency) was transfected per well. After 14h of incubation in the presence of doxycycline
610 (100 ng/mL), the cell-coated coverslip was taken and mounted carefully on a glass slide for
611 image capturing under Zeiss LSM780 confocal microscope (Carl Zeiss, Jena, Germany). All
612 samples were imaged using identical settings and were quantified as previously described [44].
613 Three biological replicates were systematically performed.
614
615 **RTqPCR and siRNA**
616 For siRNA transfection, $3.10^5$ cells per ml were seeded on 6-well plates, and 10 pmol/mL of
617 total siRNA was transfected with INTERFERin (Polyplus Transfection, France) according to
618 the manufacturer's recommendations. Total RNAs were extracted using the MACHEREY-
619 NAGEL RNA extraction kit (REF 744352.4). A total of 500 ng of RNA was converted to first-
620 strand cDNA using the RevertAid First Strand cDNA Synthesis Kit (Thermo Scientific, MA,
621 USA). Real-time qPCRs were performed in 96-well plates using the IQ SYBR Green Supermix
622 (Catalog #1708880, BioRad, CA, USA). Data were quantified using ΔΔ-Ct method and were
623 normalized to GAPDH expression. siRNA and primers sequence used in the study are
624 summarized (Table S4).
625
626 **HS27A cells differentiation, Alizarin Red staining and RNAseq**
627 ***RNA samples***
628 HS27A cells differentiation protocol toward osteoblasts was adapted from the team of Dr.
629 Véronique Maguer-Satta (Cancer Research Center of Lyon - CRCL). HS27A cells were
630 cultured in human Osteoblast differentiation media (417D-250) for 15 days. Cells undergo
631 Alizarin red stain which labels calcium deposit to verify the differentiation. For staining, cells
632 were rinsed in 1X PBS and fixed with 4% PFA for 30min. This is followed by washing cells
633 with water and staining with 2% Alizarin solution (pH 4.2) for 2-3 min. RNA was extracted
634 from cells at proliferating and differentiating states using MACHEREY-NAGEL RNA
635 extraction kit (Ref 744352.4).
636 ***Construction of the libraries and sequencing***
637 Determination of RNA concentration by fluorometric assay (Qubit4.0, Thermofisher) and
638 analysis of distribution profiles of total RNA samples by capillary electrophoresis (Tapestation
639 4150, Thermofisher) were conducted by the Sequencing platform (PSI, IGFL, Lyon). The
640 quality and quantity of the triplicate samples were satisfactory for initiating library
641 construction, with no degradation of samples observed and RIN values > 8.6. mRNA capture

642 was performed using the "NEBNext® Poly(A) mRNA Magnetic Isolation Module" protocol
643 (New England Biolabs, E7490L) with a starting material of 1µg of total RNA for each sample,
644 the various steps of the protocol having been carried out according to the supplier's
645 recommendations. Libraries were constructed using the Lexogen protocol "CORALL Total
646 RNA-Seq Library Prep Kit with UDI 12 nt Set B1" protocol (Clinisciences, 118.96) according
647 to the supplier's recommendations and from 10µl of previously purified mRNA per sample. 16
648 cycles of PCR amplification were performed to finalize the construction of indexed library.
649 The libraries were quantified (Qubit4.0, Thermofisher) and qualified (Tapestation 4150,
650 Thermofisher). Sequencing was performed on the Illumina NextSeq 500 platform using Mid
651 Output reagents with the following parameters: PE 2x81bp and 6bp index i7. A total of
652 194,006,581 reads were generated (Table S3).
653
654 ***Bioinformatics analyses***
655 Reads were mapped onto the human genome using a local pipeline derived from the one
656 supported by Lexogen (https://www.lexogen.com/corall-data-analysis/). Lexogen has made
657 their pipeline available on the Lexogen's Kangooroo app webpage
658 (https://kangooroo.com/home). In brief, UMI were first trimmed with the program umi_tools
659 extract (version 1.1.2, [45]). Adapter sequences were then removed using the Cutadapt package
660 (version 3.5, [46]) and reads quality control was performed using FastQC (version 0.11.8;
661 https://www.bioinformatics.babraham.ac.uk/projects/fastqc/). Read mapping was achieved
662 with STAR (Spliced Transcripts Alignment to a Reference, version 2.6.1a, [47]) using the
663 Homo sapiens GRCh38 genome reference (Ensembl, release 109). UMI deduplication was
664 conducted with the program umi_tools dedup (version 1.1.2, [45]) enabling the accurate
665 bioinformatic identification of PCR duplicates. The mapped reads were then quantified by Mix²
666 (version 1.4.0.1, [48]), allowing to generate a count table per sample. Differential gene
667 expression analysis was performed with DESeq2 [49] using a custom R script available on the
668 following GitLab repository: https://gitbio.ens-lyon.fr/igfl/merabet/HS27ADiff. A Docker
669 image is also provided to reproduce the results of the analysis.
670
671 **xCELLigence Assays**
672 The xCELLigence system (ACEA Biosciences Inc., San Diego, CA, USA), which records
673 cellular events in real time by measuring electrical impedance across microelectrodes
674 integrated on the bottom of culture plates (E-plates), was utilized in proliferation experiments.
675 First, HS27A cell culture media were added to each well of 16-well E-plates (ACEA

676 Biosciences Inc., San Diego, CA, USA) to measure background impedance. Then, $10.10^3$ of
677 HS27A cells were transfected with a mixture of control, 14-3-3e, TAZ, SERPINB4 siRNAs at
678 10 pmol/mL using INTERFERin (Polyplus Transfection, France) according to the
679 manufacturer's protocol. Transfected cells were directly seeded on E-plates ($5 .10^5$ cells/well),
680 and the impedance was measured every 15 min for 96 h. The impedance signal was
681 proportional to the number of cells proliferating in each well and was displayed as cell index.
682 Data were analyzed with the RTCA Software 2.0 and were presented as mean +/− SEM of
683 three experiments performed in triplicate.
684
685 **Figure legends**
686 **Figure 1: Capturing the interactome of TAZ-TurboID in HEK-293T cells. (A)** Schematic
687 representation of the capture of the interactome of TAZ-TurboID. The addition of Biotin leads
688 to the labeling of proteins in proximity of the bait protein construct. Biotinylated proteins are
689 affinity purified with streptavidin-coupled beads and analyzed by liquid chromatography
690 coupled to tandem mass spectrometry (LC-MS/MS). **(B)** Validation of the specific
691 biotinylating activity of Turbo-ID or TAZ-TurboID by immunofluorescence in HEK293T
692 cells. Biotinylation was revealed with streptavidin (SA) coupled to the 555 dye (red). The
693 expression of each construct was confirmed with an immunostaining against the HA tag present
694 in each construct (gray). Dapi (blue) stains for nuclei. Scale bar = 20 µm. **(C)** Western blot
695 analysis of biotin labeling by TurboID or TAZ-TurboID. The input and affinity purified (AP)
696 biotinylated proteins from samples expressing each construct were analyzed via western
697 blotting after biotin incubation (10 minutes). Samples were probed by streptavidin conjugate,
698 HA and Histone 3 (H3) antibodies. The band corresponding to TurboID or TAZ-TurboID is
699 indicated with anti-HA. **(D)** GO term analysis of the TAZ-TurboID interactome compared to
700 the known interactions of TAZ in the literature. The 177 novel interactions captured in this
701 study have several GO term enrichments directly or indirectly related to the Hippo signaling.
702 **(E-E')** Principle of BiFC with Venus and Cerulean derived fragments. The N-terminal
703 fragment of Venus (VN) can complement with the C-terminal fragment of Cerulean (CC) and
704 provide a Venus-like fluorescence signal. **(F)** Illustrative confocal acquisitions of BiFC
705 between VN-Taz and new candidate partners fused to CC, as indicated. Hoechst stains for
706 nuclei in live HEK293T cells (blue). Scale bar = 20 µm.
707
708 **Figure 2: Establishing Bi-nano-ID experimental parameters in HEK293T cells. (A)**
709 Principle of Bi-nano-ID. BiFC resulting from the complementation between the VN and CC

710 fragment is recognized by a GFP nanobody (csGBP) coupled to the TurboID enzyme. The
711 addition of biotin allows the biotinylation of surrounding partners, which can then be purified
712 by affinity purification (AP) and analyzed by mass spectrometry (LC-MS/MS). **(B)**
713 Simultaneous visualization of the interaction between a novel candidate partner (gray ball) and
714 each protein of the bait dimeric complex. The superposition of Venus- (green) and Cerulean-
715 like (blue) fluorescent signals in the cell is indicative of co-localized interactions, therefore of
716 trimeric complex assembly. **(C-D)** Validation of the specificity of Bi-nano-ID by
717 immunofluorescence. Biotinylation is revealed with streptavidin (SA) coupled to the 555 dye
718 (red). Interaction between the fusion TAZ and 14-3-3e (C) or TEAD2 (D) is revealed by BiFC
719 (green). Dapi stains for nuclei (blue). Enlargements highlight the specific colocalization of red
720 and green signals in the cytoplasm or the nucleus for TAZ/14-3-3e and TAZ/TEAD2
721 complexes, respectively. Scale bar = 20 µm. **(E)** Western blot of biotin labeling by TurboID.
722 Affinity purified biotinylated proteins from samples expressing dsGBP fused TurboID
723 individually or in combination with VN173-TAZ, and/or CC-14-3-3e or CC/TEAD2 were
724 analyzed via western blotting after different biotin (50 µM) incubation timepoints (10, 90, 180,
725 240 minutes), as indicated. Samples were probes by streptavidin conjugate (to reveal
726 biotinylated proteins) and GFP (to reveal the VN and CC fusion constructs). and HA antibodies
727 at (1:1000). Colored arrowheads depict sizes corresponding to VN-TAZ (blue arrowhead), CC-
728 14-3-3e (magenta arrowhead) and CC-TEAD2 (orange arrowhead). Note that parasite bands
729 with the nanobody alone are present at the size of VN-TAZ and CC-TEAD2. **(E')**
730 Quantification of the intensity of the biotinylation bands in the different conditions at 180min
731 biotin incubation time, as indicated. Quantification was obtained from three biological
732 replicates. Statistical tests were performed with one-way ANOVA (*$p < 0.05$, ****$p < 0.0001$).
733
734 **Figure 3: TAZ/14-3-3e and TAZ/TEAD2 interactome clustering. (A)** Venn diagrams
735 showing common and specific interactions between TAZ-TurboID, TAZ/14-3-3e and
736 TAZ/TEAD2 interactomes. **(B-B')** Specific interactions and GO term enrichment for TAZ/14-
737 3-3e interactome. Light pink to dark pink and magenta gradient illustrates low to medium and
738 high protein enrichment, respectively (as deduced from the lfq value of mass spectrometry data,
739 see also Table S2). **(C-C')** Specific interactions and GO term enrichment for TAZ/TEAD2-
740 interactome. Yellow to light and dark orange gradient illustrates low to medium and high
741 protein enrichment, respectively (as deduced from the lfq value of mass spectrometry data, see
742 also Table S2).
743

744 **Figure 4. Role of SERPINB3 and SERPINB4 in TAZ/14-3-3e-dependent proliferation of**
745 **HS27A mesenchymal stem cells. (A)** HS27A cells differentiate into osteoblast and are stained
746 with alizarin (red) after 15 days of culture in a osteoblast differentiation medium. **(A')**
747 Statistical Quantification of the HS27A cell alizarin staining at day 3, 7 and 15 of culture.
748 Statistical tests were performed with one-way ANOVA (****$p < 0.0001$). (B) Distribution as
749 a volcano plot of up- (Log2FC>0.5 and Log10*pvalue*>0,8) or down (Log2FC<-0.5 and
750 Log10*pvalue*>-0,8)-regulated genes during the differentiation of HS27A cells (as deduced
751 from RNA-seq. at day 1 and day 15). (C) String interactome for SERPINB4 (based on 0.15
752 interaction score of experimental evidence and database and pathway co-occurrence). (D)
753 Quantification with xCELLigence assays of HS27A cells transfected with the different siRNAs
754 as indicated. siC = siRNA control (see also Materials and Methods). Measures were performed
755 at different time points post-transfection and resulted from three independent biological
756 replicates. Two-way ANOVA with Tukey's multiple comparisons; * $p < 0.05$ and **** $p <$
757 $0.0001$.
758
759 **Figure 5: SERPINB4 forms a cooperative trimeric complex with TAZ and 14-3-3e in**
760 **living HEK293T cells. (A)** Scheme of bicolor BiFC illustrating expected Venus-and
761 Cerulean-like signals when considering the interaction of SERPINB4 with TAZ or 14-3-3e.
762 **(A')** Illustrative confocal acquisition showing the simultaneous interaction of SERPINB4 with
763 TAZ (green) or 14-3-3e (blue) in living HEK293T cells. **(A'')** Quantification of green and blue
764 fluorescent signals colocalizing in living HEK293T cells (from two independent biological
765 repliactes). **(B)** Scheme of BiFC performed between TAZ and SERPINB4 (green) when
766 affecting the expression of endogenous 14-3-3 proteins. **(B')** Illustrative confocal acquisition
767 of BiFC between TAZ and SERPINB4 (green) in the siRNA control (ctrl) condition or when
768 co-transfecting siRNA targeting endogenous *14-3-3e*, as indicated. Merge with Hoechst (blue)
769 and mCherry (green) stains for nuclei and transfection efficiency, respectively. **(B'')**
770 Quantification of the BiFC (normalized over transfection efficiency) between TAZ and
771 SERPINB4 with no siRNA (first column), control siRNA (second column) or siRNA against
772 *14-3-3e* (third column). **(C)** Scheme of BiFC performed between 14-3-3e and SERPINB4
773 (green) when co-expressing HA-tagged TAZ. **(C')** Illustrative confocal acquisition of BiFC
774 between 14-3-3e and SERPINB4 without (first column) or with HA-TAZ, as indicated. HA-
775 TAZ was revealed with an anti-HA antibody (gray) and mCherry (red) stains for transfection
776 efficiency. **(C'')** Quantification of the BiFC between14-3-3e and SERPINB4 in the absence
777 (first column) or presence (second column) of HA-TAZ. Statistical tests were performed with

778 one-way ANOVA from three biological replicates (ns: non-significant, ***$p < 0.001$,
779 **$p < 0.01$). Scale bar = 20 µm.
780
781 **Figure 6: Role of the E309 residue of TAZ as a critical interaction interface for**
782 **SERPINB4**
783 **(A)** Scheme of bicolor BiFC with the mutated $TAZ^{E309A}$ construct illustrating the expected loss
784 of Venus-like BiFC with the SERPINB4 construct and the preserved Cerulean-like BiFC
785 between SERPINB4 and 14-3-3e. **(A')** Illustrative confocal acquisition showing the loss of
786 BiFC between mutated $TAZ^{E309A}$ and SERPINB4 (green) and the preserved BiFC between
787 SERPINB4 and 14-3-3 (blue) in living HEK293T cells. mCherry (red) stains for transfection
788 efficiency in the merge picture. **(A'')** Quantification of the BiFC (normalized over transfection
789 efficiency) between wild type (1) or mutated (2) TAZ and SERPINB4, and between
790 SERPINB4 and 14-3-3e in the wild type (3) or mutated (4) TAZ co-transfection condition. (B)
791 Scheme of BiFC performed between 14-3-3e and SERPINB4 (green) when co-expressing HA-
792 tagged mutated form of TAZ. **(B')** Illustrative confocal acquisition of BiFC between 14-3-3e
793 and SERPINB4 without (first column) or with mutated HA-$TAZ^{E309A}$, as indicated. Mutated
794 HA-$TAZ^{E309A}$ was revealed with an anti-HA antibody (gray). mCherry (red) stains for
795 transfection efficiency. **(B'')** Quantification of the BiFC between14-3-3e and SERPINB4 in
796 the absence (first column) or presence of wild type (second column) or mutated (third column)
797 HA-$TAZ^{E309A}$. **(C)** Scheme of BiFC performed between mutated $TAZ^{E309A}$ and SERPINB4
798 (green) when affecting the expression of endogenous 14-3-3 proteins. **(C')** Illustrative confocal
799 acquisition of BiFC between mutated $TAZ^{E309A}$ and SERPINB4 (green) in the siRNA control
800 (ctrl) condition or when co-transfecting siRNA targeting endogenous *14-3-3e*, as indicated.
801 Merge with Hoechst (blue) and mCherry (green) stains for nuclei and transfection efficiency,
802 respectively. **(C'')** Quantification of the BiFC (normalized over transfection efficiency)
803 between mutated $TAZ^{E309A}$ and SERPINB4 with no siRNA (first column), control siRNA
804 (second column) or siRNA against *14-3-3e* (third column). Statistical tests were performed
805 with one-way ANOVA from three biological replicates (ns: non-significant, **$p < 0.01$,
806 ****$p < 0.0001$). Scale bar = 20 µm.
807
808 **Figure 7. A specific interaction mode underlies the formation of TAZ/14-3-3e/SERPINB4**
809 **trimeric complexes.** The Glu309 of TAZ is a unique contact residue for SERPINB4, being
810 responsible of the formation of a cooperative trimeric complex with 14-3-3e. The trimeric
811 TAZ/14-3-3e/SERPINB4 complex relies on specific interaction interfaces that are not used in

812 the dimeric complexes. Accordingly, the Glu309A mutation of TAZ allows the formation of a
813 dimeric complex with SERPINB4 but this dimeric complex is insensitive to 14-3-3e. Thus, the
814 binding of SERPINB4 to TAZ/14-3-3e leads to a strong remodeling of protein-protein
815 interactions. This remodeling could have incidence on the overall protein complex stability and
816 proliferation activity. Sites of contact are highlighted as well as TAZ-contacting residues with
817 14-3-3e and SERPINB4 in the dimeric and trimeric complexes (as deduced from AlphaFold
818 and Endscript predictions).
819
820 **Supplementary Figures**
821 **Supplementary Figure 1. Biotinylation activity and interactions of TAZ-TurboID in**
822 **HEK293T cells. (A)** Quantification of the SA-555 immunostaining in HEK293T cells
823 expressing TurboID or TAZ-TurboID, as indicated. **(B)** Quantification of the intensity of bands
824 revealed with the streptavidin staining in WB for TurboID and TAZ-TurboID, as indicated. **(C)**
825 Venn diagram for TAZ-TurboID specific interactions captured with the three biological
826 replicates (R1-R3). **(C')** Principal component analysis of TurboID and TAZ-TurboID
827 replicates. **(D)** Go term analysis of the 66 common interactions between TAZ-TurboID and the
828 known interactions of TAZ int the literature, and of the remaining 275 known interactions not
829 captured in this study. **(E)** Illustrative confocal acquisitions of BiFC between VN-Taz and new
830 candidate partners already known in the literature and fused to CC, as indicated. Hoechst stains
831 for nuclei in live HEK293T cells (blue). Scale bar = 20 µm.
832
833 **Supplementary Figure 2. Comparison between VN173 and VN155 for doing Bi-nano-ID.**
834 **(A)** Scheme of the complementation between VN155 or VN173 from Venus and CC from
835 Cerulean. The two complementation systems produce a Venus-like signal. **(B-B')** Comparison
836 of BiFC performed with VN173-TAZ (B) or VN155-TAZ (B'). BiFC was performed with CC-
837 14-3-3e or CC-TEAD2 in live HEK293T cells. Hoechst stains for nuclei (blue) and mCherry
838 (mCh) for transfection efficiency (red). **B''** Quantification of BiFC obtained with VN173-TAZ
839 or VN155-TAZ. BiFC was normalized over transfection efficiency in each condition.
840 Quantification was deduced from at least three biological replicates. Statistical tests were
841 performed with one-way ANOVA (****$p < 0.0001$). **(C)** Validation of the weak biotinylation
842 with BiFC performed with VN155-TAZ. Biotinylation is revealed with streptavidin (SA)
843 coupled to the 555 dye (red). Interaction between the fusion TAZ and 14-3-3e or TEAD2 is
844 revealed by BiFC (green). Dapi stains for nuclei (blue). Scale bar = 20 µm. **(C')** Quantification
845 of the biotinylation signal for each condition, as indicated. Quantification was obtained from

846 three biological replicates. Statistical tests were performed with one-way ANOVA
847 (****$p < 0.0001$).
848
849 **Supplementary Figure 3. Specificity of the csGBP nanobody for the BiFC. (A)** Fluorescent
850 immunostaining with SA-55 (red) and anti-GFP (green) recognizing the VN and CC fragment
851 with single construct transfection, as indicated. DAPI (blue) stains for nuclei. **(A')**
852 Quantification of the biotinylation signal when compared to signals obtained with BiFC
853 complexes. Quantification was obtained from three biological replicates. Statistical tests were
854 performed with one-way ANOVA (****$p < 0.0001$).
855
856 **Supplementary Figure 4.** Western blots of biotinylated proteins extracted from HEK293T
857 cells upon transfection with the different constructs, as indicated. (A) Input fraction of extracted
858 proteins revealed on WB probed by streptavidin, GFP and H3 antibodies. Colored arrowheads
859 indicate the band corresponding to VN173-TAZ (blue arrowhead), CC-14-3-3e (magenta
860 arrowhead) and CC-TEAD2 (orange arrowhead). (A') Histogram showing the quantification
861 of the biotinylation bands in each condition, as indicated. The quantification was deduced by
862 subtracting the AP band with the corresponding input band. Statistical tests were performed
863 with one-way ANOVA from three biological replicates (****$p < 0.0001$, *$p < 0.05$).
864
865 **Supplementary Figure 5. Filtering steps for identifying TAZ/14-3-3e and TAZ/TEAD2**
866 **interactomes.** Filter 1 was applied to remove BiFC interaction candidates that were also found
867 with dsGBP-TurboID alone (comparing BiFC+csGBP-TurboID to csGBP-TurboID alone in
868 the three replicates). Filter 2 identified interactions obtained with VN173-TAZ alone when
869 compared to the dsGBP-TurboID condition in each replicate. Filter 3 identified BiFC-specific
870 interactions when removing interactions found with csGBP-TurboID alone (filter 1) and VN-
871 TAZ alone (filter 2). Only interactions found in 2 or 3 replicates were considered. This filtering
872 was applied for TAZ/14-3-3e (upper panel) and TAZ/TEAD2 (lower panel) complexes, leading
873 to the identification of 96 and 42 specific interactions, respectively.
874
875 **Supplementary Figure 6. Molecular clustering of TAZ-TurboID, TAZ/14-3-3e and**
876 **TAZ/TEAD2 interactomes.**
877
878 **Supplementary Figure 7. Functional clustering of TAZ-TurboID, TAZ/14-3-3e and**
879 **TAZ/TEAD2 interactomes.** The clustering was based on GO terms that were 10 times

880 enriched at the minimum. Specific TAZ/14-3-3e and TAZ/TEAD2 Go term enrichments are
881 shown in the Fig. 3.
882
883 **Supplementary Figure 8. (A)** Protein sequence alignment of SERPINB3 and SERPINB4. **(B)**
884 Effect of siRNAs targeting *SERPINB3* and *SERPINB4* on endogenous *SERPINB3* in HS27A
885 cells. **(C)** Effect of siRNAs targeting *SERPINB3* and *SERPINB4* on endogenous *SERPINB4* in
886 HS27A cells. **(D)** Effect of siRNAs targeting *14-3-3* on endogenous *SERPINB4* expression in
887 HS27A cells. **(E)** Effect of siRNAs targeting *TAZ* on endogenous *SERPINB4* expression in
888 HS27A cells. **(F)** Effect of siRNAs targeting *14-3-3* on endogenous *SERPINB4* expression in
889 HEK293T cells. **(G-G'')** Effects of siRNAs targeting *TAZ* (G), *14-3-3e* (G') or *SERPINB3/B4*
890 (G'') on endogenous *TAZ* expression in HS27A cells. **(H)** Effects of siRNAs targeting *14-3-3e*
891 on endogenous *TAZ* expression in HEK293T cells. **(I-I'')** Effects of siRNAs targeting *TAZ* (I),
892 *14-3-3e* (I') or *SERPINB3/B4* (I'') on endogenous *14-3-3e* expression in HS27A cells. **(J)**
893 Effects of siRNAs targeting *14-3-3e* on endogenous *14-3-3e* expression in HEK293T cells.
894 Graphs result from the quantification of RTqPCR from three biological replicates in each
895 condition. Statistical tests were performed with one-way ANOVA (ns: non-significant,
896 $^{**}p < 0.01$, $^{****}p < 0.0001$).
897
898 **Supplementary Figure 9. The residue Glu309 of TAZ is critical to recruit SERPINB4 in**
899 **the context of the trimeric association with 14-3-3e. (A)** AlphaFold prediction of TAZ/14-
900 3-3e/SERPINB4 trimeric complex. Enlargement highlights key residues of TAZ involved in
901 the interaction with SERPINB4 (Glu309) and 14-3-3e (Asp308). **(B)** Endscript-2 prediction of
902 all contacts established between the three partners in the TAZ/14-3-3e/SERPINB4 trimeric
903 complex (https://endscript.ibcp.fr/ESPript/ENDscript/index.php). Accessibility (acc, white to
904 cyan and blue indicates not to mildly or highly accessible, respectively), hydrophobicity (hyd)
905 and beta-sheet or alpha-helical structures are indicated below or above the sequence. Residues
906 involved in contacts inferior to 3,3A or in contact between 3,3 and 5A are highlighted with a
907 red or black letter, respectively. **(C)** Prediction of disordered regions (red line above the gray
908 line), ordered domain (blue box), short linear interaction motifs (violet boxes) and LAT1-
909 phosphorylation sites in TAZ protein sequence. Adapted from ELM
910 (http://elm.eu.org/search.html) and IUPred2A (https://iupred2a.elte.hu/). **(D-D')**
911 Quantification of wild type or mutated TAZ expression in HEK293T cells. VN-fusion
912 constructs were revealed with anti-GFP (green). Dapi stains for nuclei (D). Quantification from
913 three biological replicates shows similar expression levels of wild type and mutated VN-fusion

914 TAZ constructs (D'). Statistical tests were performed with one-way ANOVA
915 (****$p < 0.0001$). **(E-E').** Quantification of normalized BiFC (over mCherry, red) between
916 SERPINB4 and wild type TAZ (green, column 1 in E') and 14-3-3e (blue, column 2 in E').
917
918 **Supplementary Figure 10. AlphaFold (A) and Endscript2 (B) prediction of TAZ/14-3-3e**
919 **dimeric protein complex.**
920
921 **Supplementary Figure 11. AlphaFold (A) and Endscript2 (B) prediction of**
922 **TAZ/SERPINB4 dimeric protein complex.**
923
924 **Supplementary Figure 12. AlphaFold (A) and Endscript2 (B) prediction of 14-3-**
925 **3e/SERPINB4 dimeric protein complex.**
926
927 **Supplementary Tables**
928 **Supplementary Table 1. RNA-seq data of HEK293T cells.**
929
930 **Supplementary Table 2. Mass spectrometry data and GO term enrichment for TAZ-**
931 **TurboID**
932
933 **Supplementary Table 3. Mass spectrometry data and GO term enrichment for TAZ/14-**
934 **3-3e and TAZ/TEAD2 complexes**
935
936 **Supplementary Table 4. RNA-seq data of HS27A cells.**
937
938 **Supplementary Table 5. Sequences of oligonucleotides and primers used in this study for**
939 **cloning and RTqPCRs**
940
941 **Authors contribution**
942 S.M. designed the study. N.H.S. performed the experiments and acquired the data. J.C. and
943 N.H.S., with the support of S.M. and F.D., were responsible of proteomics data analyses. N.H.S
944 and L.G. analyzed the RNA-seq data. Y.J. was responsible for the cytoscape network
945 illustration. S.M. and N.H.S. wrote the paper and J.C., L.G. and F.D. amended it.
946
947 **Acknowledgments**

948 We are beyond grateful for the help of Christelle FORCET in performing the proliferation
949 assay and support at the experimental level. We thank also Benjamin GILLET, Sandrine
950 HUGHES and Julien DELLINGER for the RNA-seq preparation and valuable help in the
951 transcriptomic analyses. We thank Adeline PAGE from the Protein Science Facility at the SFR
952 bioscience (UAR3444/CNRS, US8/Inserm, ENS de Lyon) for Mass spectrometry analyses. We
953 are very grateful for the help provided by Sylvain LEFORT and the team of Dr. Veronique
954 Maguer-Satta (CRCL) for HS27A line and culturing tips. We thank Alain GUIGNANDON
955 and Daniel BOUVARD for their valuable inputs in the project. This project was supported by
956 Ambition Pack from the Region Rhone Alpes and the Foundation of Medical Research (FRM
957 #FDT202304016377, 4th year grant for N.H.S).
958

959 **References**

960 1. Holguin-Cruz JA, Foster LJ, G.J. Where protein structure and cell diversity meet.
961 *Trends Cell Biol.* **2022**, *Dec;32*, 996–1007, doi:10.1016/j.tcb.2022.04.004.
962 2. Schaefer MH, Lopes TJ, Mah N, Shoemaker JE, Matsuoka Y, Fontaine JF, Louis-
963 Jeune C, Eisfeld AJ, Neumann G, Perez-Iratxeta C, Kawaoka Y, Kitano H, A.-N.M.
964 Adding protein context to the human protein-protein interaction network to reveal
965 meaningful interactions. *PLoS Comput Biol.* **2013**, *9(1)*,
966 doi:10.1371/journal.pcbi.1002860.
967 3. Liu X, Abad L, Chatterjee L, Cristea IM, V.M. Mapping protein-protein interactions
968 by mass spectrometry. *Mass Spectrom Rev.* **2024**, *May 14*, doi:10.1002/mas.21887.
969 4. Branon TC, Bosch JA, Sanchez AD, Udeshi ND, Svinkina T, Carr SA, Feldman JL,
970 Perrimon N, T.A. Efficient proximity labeling in living cells and organisms with
971 TurboID. *Nat Biotechnol.* **2018**, *Oct 36*, 880–887, doi:10.1038/nbt.4201.
972 5. Cho KF, Branon TC, Rajeev S, Svinkina T, Udeshi ND, Thoudam T, Kwak C, Rhee
973 HW, Lee IK, Carr SA, T.A. Split-TurboID enables contact-dependent proximity
974 labeling in cells. *Proc Natl Acad Sci U S A.* **2020**, *Jun 2*, 12143–12154,
975 doi:10.1073/pnas.1919528117.
976 6. Takano T, Wallace JT, Baldwin KT, Purkey AM, Uezu A, Courtland JL, Soderblom
977 EJ, Shimogori T, Maness PF, Eroglu C, S.S. Chemico-genetic discovery of astrocytic
978 control of inhibition in vivo. *Nature* **2020**, *Dec;588*, 296–3027837,
979 doi:10.1038/s41586-020-2926-0.
980 7. Takano T, S.S. Tripartite synaptomics: Cell-surface proximity labeling in vivo.
981 *Neurosci Res.* **2021**, *Dec*, 14–21, doi:10.1016/j.neures.2021.05.002.

982 8. Barroso-Gomila O, Trulsson F, Muratore V, Canosa I, Merino-Cacho L, Cortazar AR,
983 Pérez C, Azkargorta M, Iloro I, Carracedo A, Aransay AM, Elortza F, Mayor U,
984 Vertegaal ACO, Barrio R, S.J. Identification of proximal SUMO-dependent interactors
985 using SUMO-ID. *Nat. Commun.* **2021**, *12*, 6671, doi:10.1038/s41467-021-26807-6.
986 9. Panciera T, Azzolin L, Cordenonsi M, P.S. Mechanobiology of YAP and TAZ in
987 physiology and disease. *Nat Rev Mol Cell Biol.* **2017**, *Dec;18*, 758–770,
988 doi:10.1038/nrm.2017.87.
989 10. Fu M, Hu Y, Lan T, Guan KL, Luo T, L.M. The Hippo signalling pathway and its
990 implications in human health and diseases. *Signal Transduct Target Ther.* **2022**, *Nov 8*,
991 376, doi:10.1038/s41392-023-01682-3.
992 11. Yang W, Han W, Qin A, Wang Z, Xu J, Q.Y. The emerging role of Hippo signaling
993 pathway in regulating osteoclast formation. *J Cell Physiol.* **2018**, *Jun;233*, 4606–4617,
994 doi:10.1002/jcp.26372.
995 12. Kovar H, Bierbaumer L, R.-S.B. The YAP/TAZ Pathway in Osteogenesis and Bone
996 Sarcoma Pathogenesis. *Cells* **2020**, *Apr 15;9*, 972, doi:10.3390/cells9040972.
997 13. Ren H, Ou Q, Pu Q, Lou Y, Yang X, Han Y, L.S. Comprehensive Review on
998 Bimolecular Fluorescence Complementation and Its Application in Deciphering
999 Protein-Protein Interactions in Cell Signaling Pathways. *Biomolecules.* **2024**, *Jul 17*,
1000 859, doi:10.3390/biom14070859.
1001 14. Ariotti, N.; Rae, J.; Giles, N.; Martel, N.; Sierecki, E.; Gambin, Y.; Hall, T.E.; Parton,
1002 R.G. Ultrastructural localisation of protein interactions using conditionally stable
1003 nanobodies. *PLoS Biol.* **2018**, *16*, doi:10.1371/journal.pbio.2005473.
1004 15. Croucher DR, Iconomou M, Hastings JF, Kennedy SP, Han JZ, Shearer RF, McKenna
1005 J, Wan A, Lau J, Aparicio S, S.D. Bimolecular complementation affinity purification
1006 (BiCAP) reveals dimer-specific protein interactions for ERBB2 dimers. *Sci Signal.*
1007 **2016**, *Jul 12;9*, doi:10.1126/scisignal.aaf0793.
1008 16. Hu, C.-D.; Kerppola, T.K. Simultaneous visualization of multiple protein interactions
1009 in living cells using multicolor fluorescence complementation analysis. *Nat.*
1010 *Biotechnol.* **2003**, *21*, 539–45, doi:10.1038/nbt816.
1011 17. Kerppola, T.K. Multicolor bimolecular fluorescence complementation (BiFC) analysis
1012 of protein interactions with alternative partners. *Cold Spring Harb. Protoc.* **2013**,
1013 *2013*, 798–803, doi:10.1101/pdb.top077164.
1014 18. Nagai, T.; Ibata, K.; Park, E.S.; Kubota, M.; Mikoshiba, K.; Miyawaki, A. A variant of
1015 yellow fluorescent protein with fast and efficient maturation for cell-biological

1016 applications. *Nat. Biotechnol.* **2002**, *20*, 87–90, doi:10.1038/nbt0102-87.
1017 19. Rizzo, M. a; Springer, G.H.; Granada, B.; Piston, D.W. An improved cyan fluorescent
1018 protein variant useful for FRET. *Nat. Biotechnol.* **2004**, *22*, 445–9,
1019 doi:10.1038/nbt945.
1020 20. Zeng L, Wang WH, Arrington J, Shao G, Geahlen RL, Hu CD, T.W. Identification of
1021 Upstream Kinases by Fluorescence Complementation Mass Spectrometry. *ACS Cent*
1022 *Sci.* **2017**, *Oct 25;3*, 1078–1085.
1023 21. Abenza JF, Rossetti L, Mouelhi M, Burgués J, Andreu I, Kennedy K, Roca-Cusachs P,
1024 Marco S, García-Ojalvo J, T.X. Mechanical control of the mammalian circadian clock
1025 via YAP/TAZ and TEAD. *J Cell Biol.* **2023**, *Sep 4;222*, e202209120.,
1026 doi:e202209120.
1027 22. Shen H, Huang X, Zhao Y, Wu D, Xue K, Yao J, Wang Y, Tang N, Q.Y. The Hippo
1028 pathway links adipocyte plasticity to adipose tissue fibrosis. *Nat Commun.* **2022**, *Oct*
1029 *13;13*, 6030, doi:10.1038/s41467-022-33800-0.
1030 23. Yuan Y, Park J, Feng A, Awasthi P, Wang Z, Chen Q, I.-B.R. YAP1/TAZ-TEAD
1031 transcriptional networks maintain skin homeostasis by regulating cell proliferation and
1032 limiting KLF4 activity. *Nat Commun.* **2020**, *Mar 19;11*, 1472, doi:10.1038/s41467-
1033 020-15301-0.
1034 24. Du Z, Shi X, G.A. lncRNA H19 facilitates the proliferation and differentiation of
1035 human dental pulp stem cells via EZH2-dependent LATS1 methylation. *Mol Ther*
1036 *Nucleic Acids.* **2021**, *Apr 24*, 116–126, doi:10.1016/j.omtn.2021.04.017.
1037 25. Driskill JH, P.D. Control of stem cell renewal and fate by YAP and TAZ. *Nat Rev Mol*
1038 *Cell Biol.* **2023**, *Dec;24*, 895–911, doi:10.1038/s41580-023-00644-5.
1039 26. Luo J, L.P. Context-dependent transcriptional regulations of YAP/TAZ in stem cell
1040 and differentiation. *Stem Cell Res Ther.* **2022**, *Jan 10;13(*, doi:10.1186/s13287-021-
1041 02686-y.
1042 27. Roecklein BA, T.-S.B. Functionally distinct human marrow stromal cell lines
1043 immortalized by transduction with the human papilloma virus E6/E7 genes. *Blood*
1044 **1995**, *Feb 15;85*, 997–1005.
1045 28. Liu B, Wu S, Han L, Z.C. β-catenin signaling induces the osteoblastogenic
1046 differentiation of human pre-osteoblastic and bone marrow stromal cells mainly
1047 through the upregulation of osterix expression. *Int J Mol Med.* **2015**, *Dec;36*, 1572–82,
1048 doi:10.3892/ijmm.
1049 29. Murakami A, Nakagawa T, Kaneko M, Nawata S, Takeda O, Kato H, S.N.

1050 Suppression of SCC antigen promotes cancer cell invasion and migration through the
1051 decrease in E-cadherin expression. *Int J Oncol.* **2006**, *Nov;29*, 1231–5.
1052 30. Zhang Y, Wang L, Sun X, L.F. SERPINB4 Promotes Keratinocyte Inflammation via
1053 p38MAPK Signaling Pathway. *J Immunol Res.* **2023**, *Mar 21*,
1054 doi:10.1155/2023/3397940.
1055 31. Rigiracciolo DC, Nohata N, Lappano R, Cirillo F, Talia M, Adame-Garcia SR, Arang
1056 N, Lubrano S, De Francesco EM, Belfiore A, Gutkind JS, M.M. Focal Adhesion
1057 Kinase (FAK)-Hippo/YAP transduction signaling mediates the stimulatory effects
1058 exerted by S100A8/A9-RAGE system in triple-negative breast cancer (TNBC). *J Exp*
1059 *Clin Cancer Res.* **2022**, *Jun 3;41(1*, doi:10.1186/s13046-022-02396-0.
1060 32. Jumper J, Evans R, Pritzel A, Green T, Figurnov M, Ronneberger O, Tunyasuvunakool
1061 K, Bates R, Žídek A, Potapenko A, Bridgland A, Meyer C, Kohl SAA, Ballard AJ,
1062 Cowie A, Romera-Paredes B, Nikolov S, Jain R, Adler J, Back T, Petersen S, Reiman
1063 D, Clancy E, H.D. Highly accurate protein structure prediction with AlphaFold. *Nature*
1064 **2021**, *Aug;596*, 583–589, doi:10.1038/s41586-021-03819-2.
1065 33. Robert X, G.P. Deciphering key features in protein structures with the new ENDscript
1066 server. *Nucleic Acids Res.* **2014**, *Jul;42*, doi:10.1093/nar/gku316.
1067 34. Morsut, L.; Dupont, S.; Morsut, L.; Aragona, M.; Enzo, E.; Giulitti, S.; Cordenonsi, M.
1068 Role of YAP/TAZ in mechanotransduction. *Nature* **2011**, *474*, 179–183,
1069 doi:10.1038/nature10137.
1070 35. Kumar, M.; Gouw, M.; Michael, S.; Sámano-Sánchez, H.; Pancsa, R.; Glavina, J.;
1071 Diakogianni, A.; Valverde, J.A.; Bukirova, D.; Čalyševa, J.; et al. ELM—the
1072 eukaryotic linear motif resource in 2020. *Nucleic Acids Res.* **2019**,
1073 doi:10.1093/nar/gkz1030.
1074 36. Mészáros, B.; Erdős, G.; Dosztányi, Z. IUPred2A: context-dependent prediction of
1075 protein disorder as a function of redox state and protein binding. *Nucleic Acids Res.*
1076 **2018**, *46*, W329–W337, doi:10.1093/nar/gky384.
1077 37. De Munter, S.; Görnemann, J.; Derua, R.; Lesage, B.; Qian, J.; Heroes, E.; Waelkens,
1078 E.; Van Eynde, A.; Beullens, M.; Bollen, M. Split-BioID: a proximity biotinylation
1079 assay for dimerization-dependent protein interactions. *FEBS Lett.* 2017, *591*, 415–424.
1080 38. Schopp IM, Amaya Ramirez CC, Debeljak J, Kreibich E, Skribbe M, Wild K, B.J.
1081 Split-BioID a conditional proteomics approach to monitor the composition of
1082 spatiotemporally defined protein complexes. *Nat Commun.* **2017**, *Jun 6;8*,
1083 doi:10.1038/ncomms15690.

1084 39. Cox J, Neuhauser N, Michalski A, Scheltema RA, Olsen JV, M.M. Andromeda: a
1085 peptide search engine integrated into the MaxQuant environment. *J Proteome Res.*
1086 **2011**, *Apr 1;10*, 1794–805, doi:10.1021/pr101065j.
1087 40. Tyanova S, Temu T, C.J. The MaxQuant computational platform for mass
1088 spectrometry-based shotgun proteomics. *Nat Protoc.* **2016**, *Dec;11*, 2301–2319,
1089 doi:10.1038/nprot.2016.136.
1090 41. Szklarczyk D, Gable AL, Nastou KC, Lyon D, Kirsch R, Pyysalo S, Doncheva NT,
1091 Legeay M, Fang T, Bork P, Jensen LJ, von M.C. The STRING database in 2021:
1092 customizable protein-protein networks, and functional characterization of user-
1093 uploaded gene/measurement sets. *Nucleic Acids Res.* **2021**, *Jan 8;49*, D605–D612,
1094 doi:10.1093/nar/gkaa1074.
1095 42. Shannon, P., Markiel, A., Ozier, O., Baliga, N.S., Wang, J.T., Ramage, D., Amin, N.,
1096 Schwikowski, B., and Ideker, T. Shannon, P., Markiel, A., Ozier, O., Baliga, N.S.,
1097 Wang, J.T., Ramage, D., Amin, N., Schwikowski, B., and Ideker, T. Cytoscape: a
1098 software environment for integrated models of biomolecular interaction networks.
1099 *Genome Res.* **2003**, *13*, 2498–2504.
1100 43. Thomas PD, Ebert D, Muruganujan A, Mushayahama T, Albou LP, M.H. PANTHER:
1101 Making genome-scale phylogenetics accessible to all. *Protein Sci.* **2022**, *Jan;31*, 8–22,
1102 doi:10.1002/pro.4218.
1103 44. Jia Y, Reboulet J, Gillet B, Hughes S, Forcet C, Tribollet V, Hajj Sleiman N, Kundlacz
1104 C, Vanacker JM, Bleicher F, M.S. A Live Cell Protein Complementation Assay for
1105 ORFeome-Wide Probing of Human HOX Interactomes. *Cells* **2023**, *12*, 200,
1106 doi:10.3390/cells12010200.
1107 45. Smith T, Heger A, S.I. UMI-tools: modeling sequencing errors in Unique Molecular
1108 Identifiers to improve quantification accuracy. *Genome Res.* **2017**, *Mar;27*, 491–499,
1109 doi:10.1101/gr.209601.116.
1110 46. Kechin A, Boyarskikh U, Kel A, F.M. cutPrimers: A New Tool for Accurate Cutting
1111 of Primers from Reads of Targeted Next Generation Sequencing. *J Comput Biol.* **2017**,
1112 *Nov;24*, 1138–1143, doi:10.1089/cmb.2017.0096.
1113 47. Dobin A, Davis CA, Schlesinger F, Drenkow J, Zaleski C, Jha S, Batut P, Chaisson M,
1114 G.T. STAR: ultrafast universal RNA-seq aligner. *Bioinformatics.* **2013**, *Jan 1;29*, 15–
1115 21, doi:10.1093/bioinformatics/bts635.
1116 48. Anders S, Pyl PT, H.W. HTSeq--a Python framework to work with high-throughput
1117 sequencing data. *Bioinformatics.* **2015**, *Jan 15;31*, 166–9,

1118 doi:10.1093/bioinformatics/btu638.
1119 49. Love MI, Huber W, A.S. Moderated estimation of fold change and dispersion for
1120 RNA-seq data with DESeq2. *Genome Biol.* **2014**, *15(12)*, doi:10.1186/s13059-014-
1121 0550-8.
1122

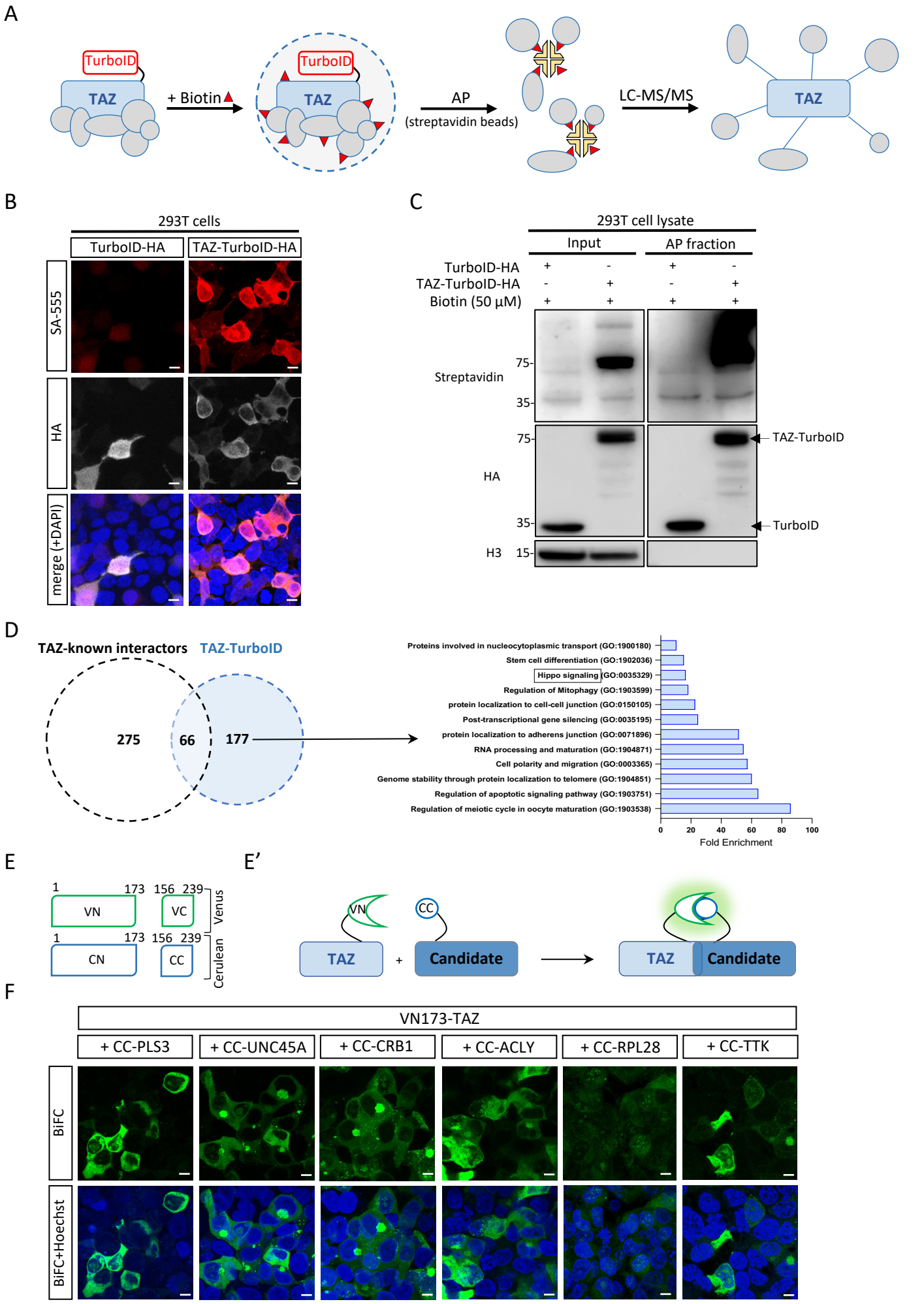
A
TurboID
TAZ
+ Biotin
TurboID
TAZ
AP
(streptavidin beads)
LC-MS/MS
TAZ
B
293T cells
TurboID-HA
TAZ-TurboID-HA
SA-555
HA
merge (+DAPI)
C
293T cell lysate
Input
AP fraction
TurboID-HA
TAZ-TurboID-HA
Biotin (50 µM)
Streptavidin
75-
35-
HA
75-
35-
TAZ-TurboID
TurboID
H3
15-
D
TAZ-known interactors
TAZ-TurboID
275
66
177
Proteins involved in nucleocytoplasmic transport (GO:1900180)
Stem cell differentiation (GO:1902036)
Hippo signaling (GO:0035329)
Regulation of Mitophagy (GO:1903599)
protein localization to cell-cell junction (GO:0150105)
Post-transcriptional gene silencing (GO:0035195)
protein localization to adherens junction (GO:0071896)
RNA processing and maturation (GO:1904871)
Cell polarity and migration (GO:0003365)
Genome stability through protein localization to telomere (GO:1904851)
Regulation of apoptotic signaling pathway (GO:1903751)
Regulation of meiotic cycle in oocyte maturation (GO:1903538)
0
20
40
60
80
100
Fold Enrichment
E
1
173
156
239
VN
VC
Venus
1
173
156
239
CN
CC
Cerulean
E'
VN
CC
TAZ
+
Candidate
TAZ
Candidate
F
VN173-TAZ
+ CC-PLS3
+ CC-UNC45A
+ CC-CRB1
+ CC-ACLY
+ CC-RPL28
+ CC-TTK
BiFC
BiFC+Hoechst

Figure 1

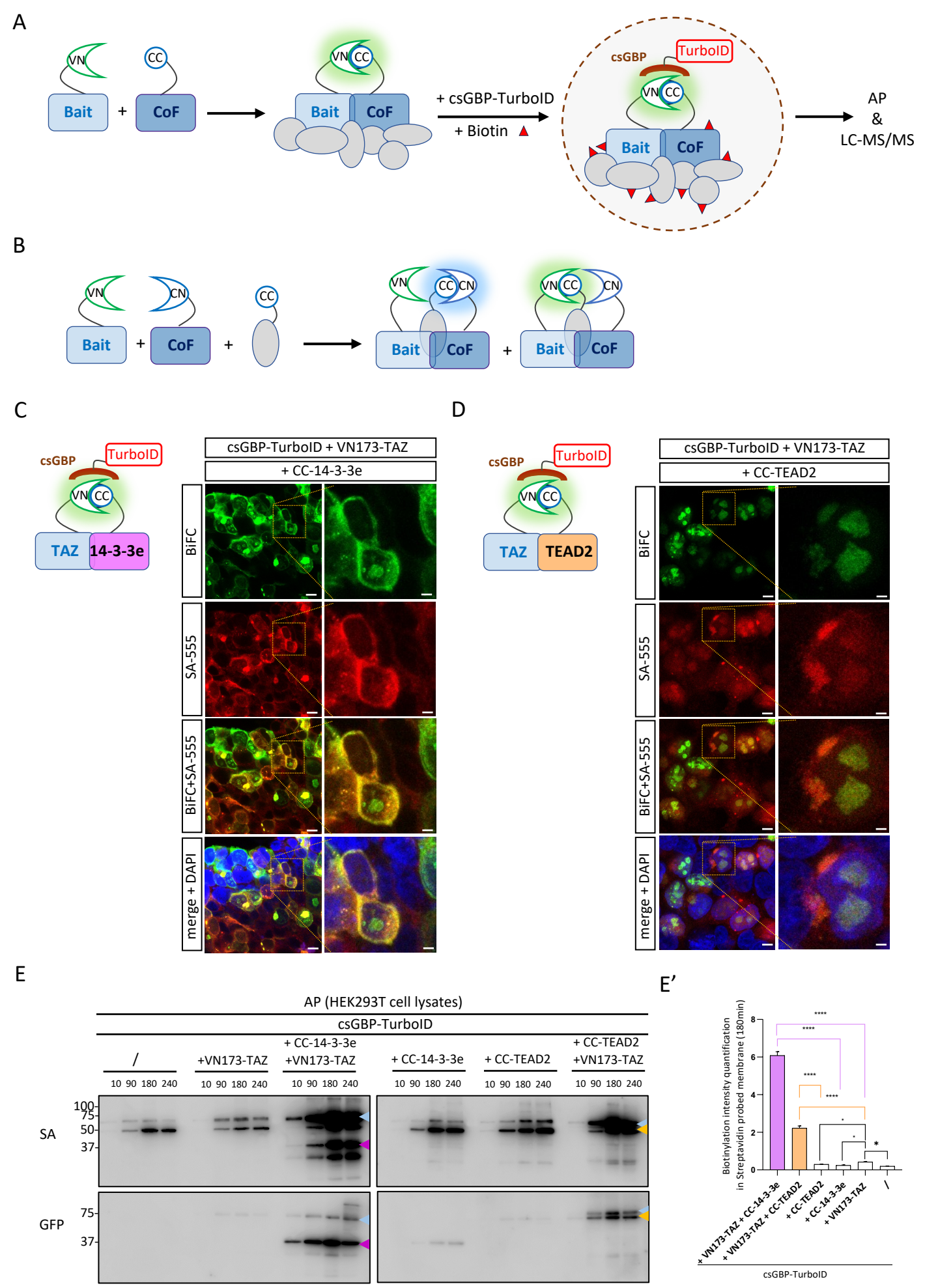
A
VN
CC
Bait
CoF
+ csGBP-TurboID
+ Biotin
csGBP
TurboID
AP
&
LC-MS/MS
B
CN
C
csGBP
TurboID
TAZ
14-3-3e
csGBP-TurboID + VN173-TAZ
+ CC-14-3-3e
BiFC
SA-555
BiFC+SA-555
merge + DAPI
D
TEAD2
+ CC-TEAD2
E
AP (HEK293T cell lysates)
csGBP-TurboID
/
+VN173-TAZ
+ CC-14-3-3e
+VN173-TAZ
+ CC-TEAD2
10 90 180 240
SA
GFP
100
75
50
37
E'
Biotinylation intensity quantification
in Streptavidin probed membrane (180min)
+ VN173-TAZ + CC-14-3-3e
+ VN173-TAZ + CC-TEAD2
+ CC-TEAD2
+ CC-14-3-3e
+ VN173-TAZ
csGBP-TurboID

Figure 2

A

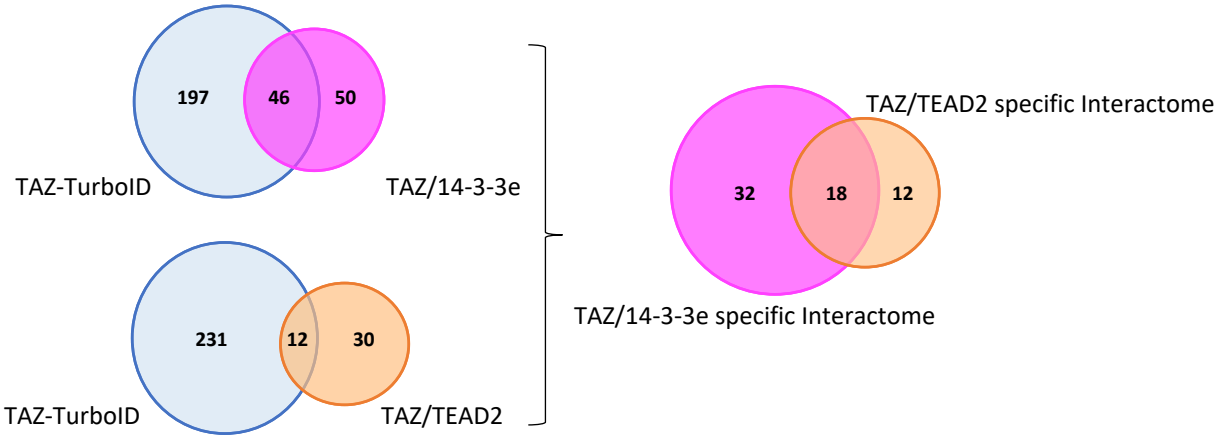


B

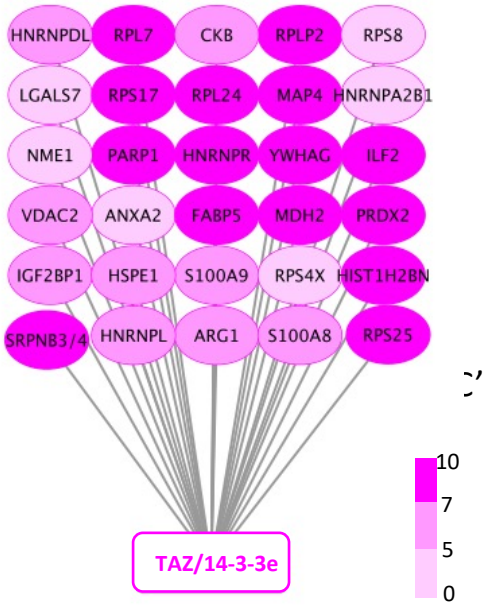


B'

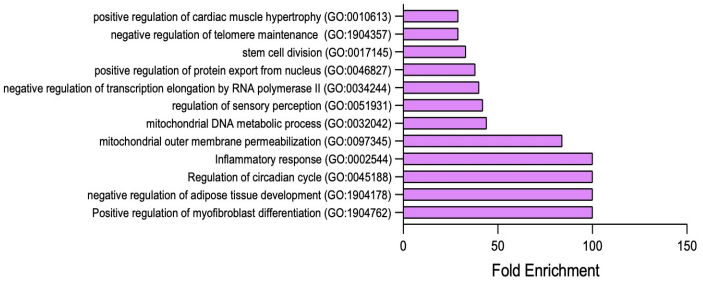


C

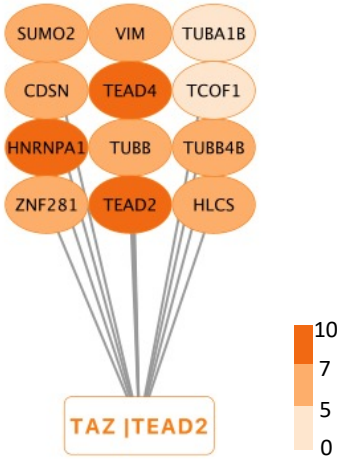


C'

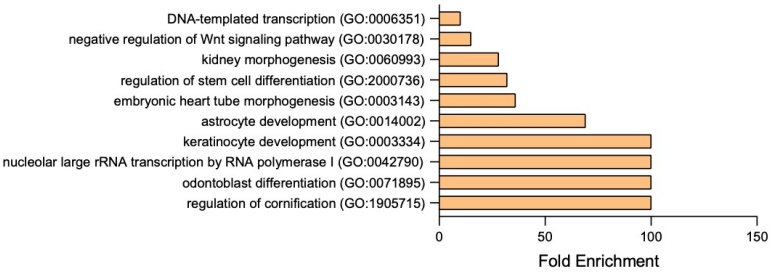


Figure 3

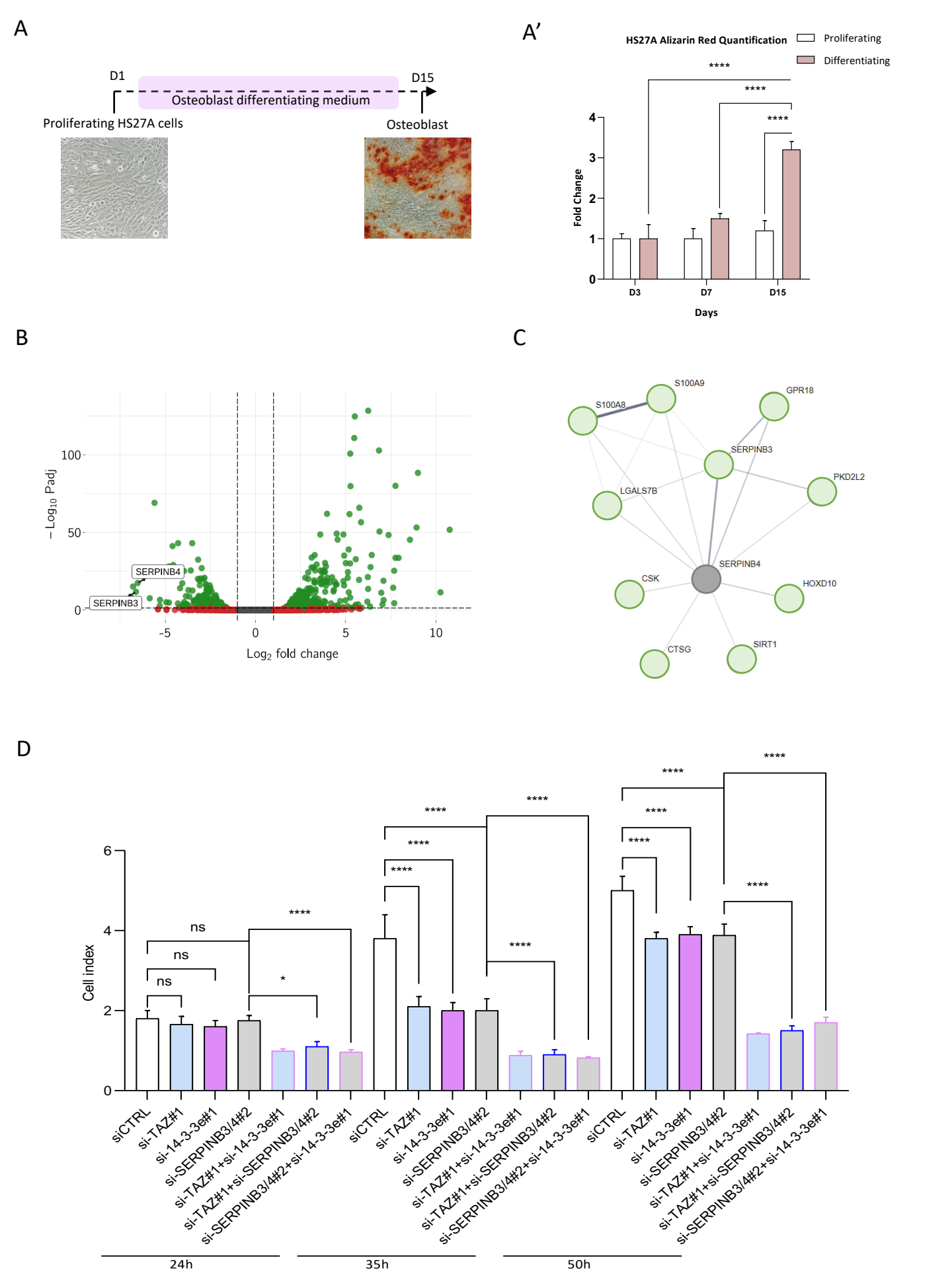
A
D1
D15
Osteoblast differentiating medium
Proliferating HS27A cells
Osteoblast
A'
HS27A Alizarin Red Quantification
Proliferating
Differentiating
Fold Change
Days
D3
D7
D15
B
SERPINB4
SERPINB3
Log2 fold change
C
S100A9
S100A8
GPR18
SERPINB3
PKD2L2
LGALS7B
SERPINB4
CSK
HOXD10
CTSG
SIRT1
D
Cell index
siCTRL
si-TAZ#1
si-14-3-3e#1
si-SERPINB3/4#2
si-TAZ#1+si-14-3-3e#1
si-TAZ#1+si-SERPINB3/4#2
si-SERPINB3/4#2+si-14-3-3e#1
24h
35h
50h

Figure 4

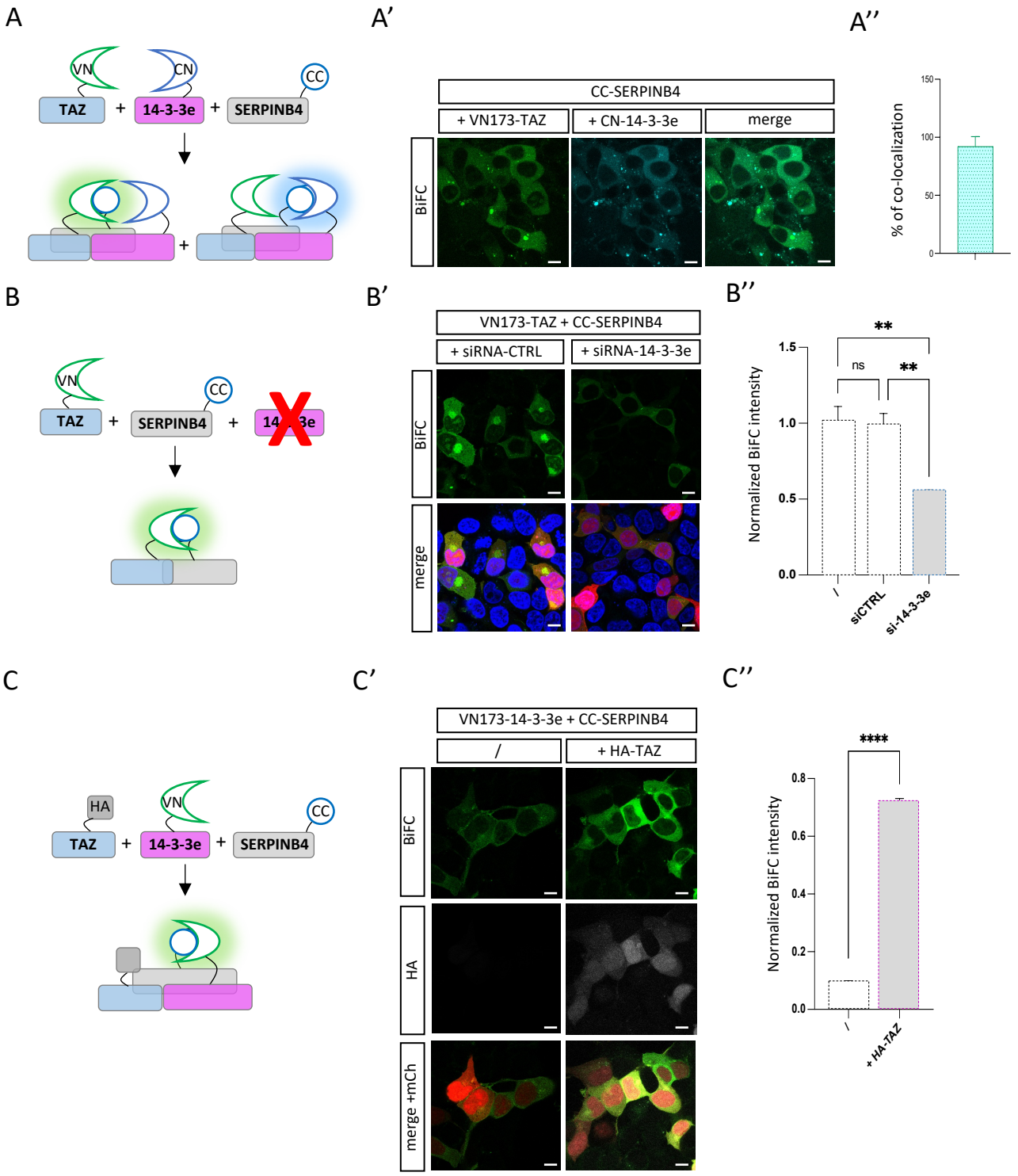
A
VN
CN
CC
TAZ
14-3-3e
SERPINB4
A'
CC-SERPINB4
+ VN173-TAZ
+ CN-14-3-3e
merge
BiFC
A''
% of co-localization
150
100
50
0
B
VN
CC
TAZ
SERPINB4
B'
VN173-TAZ + CC-SERPINB4
+ siRNA-CTRL
+ siRNA-14-3-3e
BiFC
merge
B''
**
ns
**
Normalized BiFC intensity
1.5
1.0
0.5
0.0
/
siCTRL
si-14-3-3e
C
HA
VN
CC
TAZ
14-3-3e
SERPINB4
C'
VN173-14-3-3e + CC-SERPINB4
/
+ HA-TAZ
BiFC
HA
merge +mCh
C''
****
Normalized BiFC intensity
0.8
0.6
0.4
0.2
0.0
/
+ HA-TAZ

Figure 5

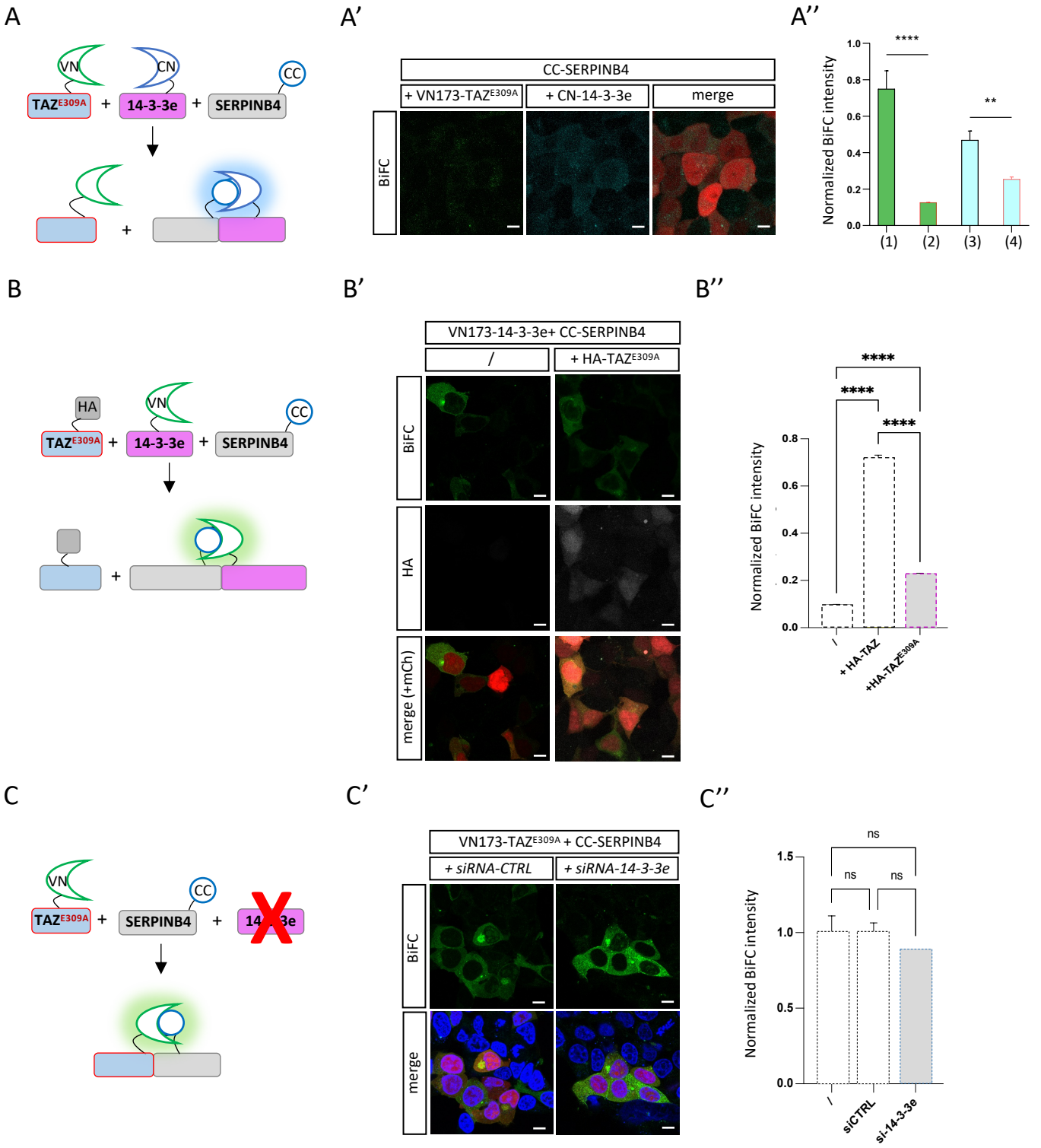
A
VN
CN
CC
TAZE309A
+
14-3-3e
+
SERPINB4
A'
CC-SERPINB4
+ VN173-TAZE309A
+ CN-14-3-3e
merge
BiFC
A''
Normalized BiFC intensity
****
**
(1)
(2)
(3)
(4)
B
HA
VN
CC
TAZE309A
+
14-3-3e
+
SERPINB4
B'
VN173-14-3-3e+ CC-SERPINB4
/
+ HA-TAZE309A
BiFC
HA
merge (+mCh)
B''
Normalized BiFC intensity
****
****
****
/
+ HA-TAZ
+HA-TAZE309A
C
VN
CC
TAZE309A
+
SERPINB4
+
C'
VN173-TAZE309A + CC-SERPINB4
+ siRNA-CTRL
+ siRNA-14-3-3e
BiFC
merge
C''
Normalized BiFC intensity
ns
ns
ns
/
siCTRL
si-14-3-3e

Figure 6

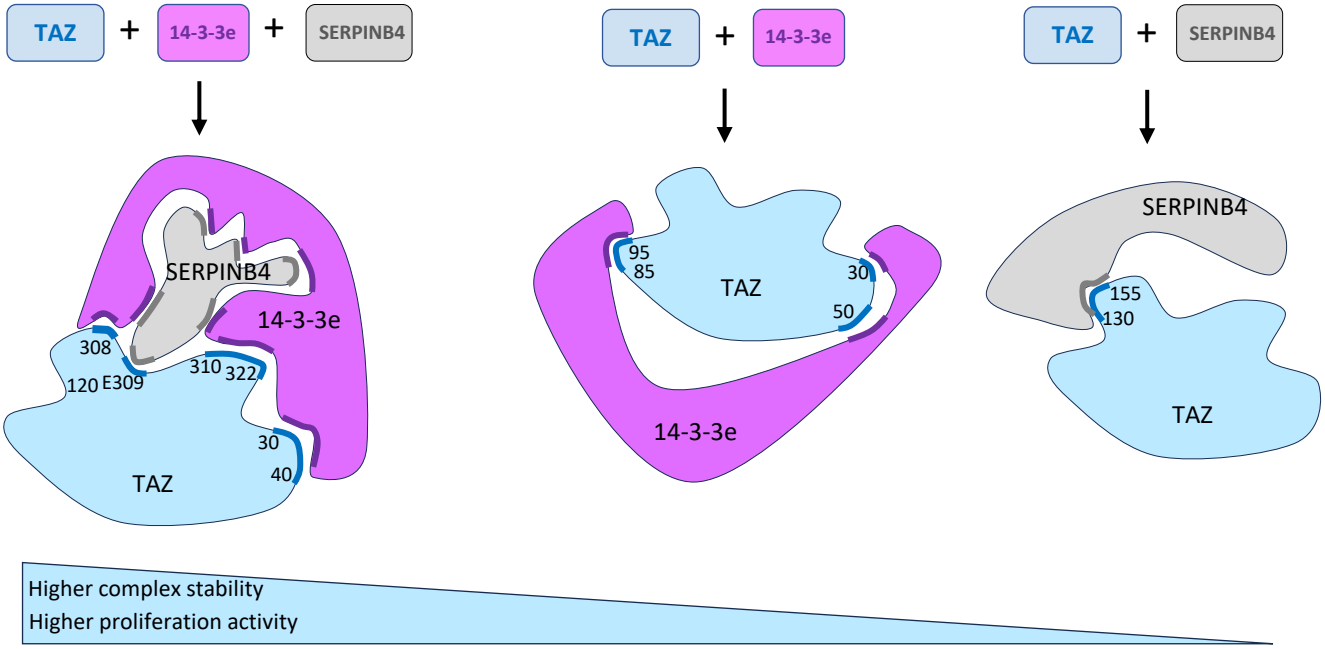
TAZ
+
14-3-3e
+
SERPINB4
SERPINB4
14-3-3e
308
120
E309
310
322
30
40
TAZ
TAZ
+
14-3-3e
95
85
TAZ
30
50
14-3-3e
TAZ
+
SERPINB4
SERPINB4
155
130
TAZ
Higher complex stability
Higher proliferation activity

Figure 7